

1 **Revision 1-shortened version**

2 **Magma oxygen fugacity of mafic-ultramafic intrusions in**
3 **convergent margin settings: insights for the role of magma**
4 **oxidation states on magmatic Ni-Cu sulfide mineralization**

5

6

7 Yonghua Cao^{1,2}, Christina Yan Wang^{1,2*}, Bo Wei^{1,2}

8 ¹ CAS Key Laboratory of Mineralogy and Metallogeny, Guangzhou Institute of
9 Geochemistry, Chinese Academy of Sciences, Guangzhou 510640, China

10 ² Guangdong Provincial Key Laboratory of Mineral Physics and Materials, Guangzhou
11 510640, China

12

13

14

15

16

17 Corresponding author: Dr. C.Y. Wang (wang_yan@gig.ac.cn)

18

Abstract

19 Oxygen fugacities (fO_2) of mantle-derived mafic magmas have important controls on
20 the sulfur status and solubility of the magmas, which are key factors to the formation of
21 magmatic Ni-Cu sulfide deposits, particularly those in convergent margin settings. In
22 order to investigate the fO_2 of mafic magmas related to Ni-Cu sulfide deposits in
23 convergent margin settings, we obtained the magma fO_2 of a number of Ni-Cu sulfide-
24 bearing mafic-ultramafic intrusions in the central Asian orogenic belt (CAOB), North
25 China, based on the olivine-spinel oxygen barometer and the modeling of V partitioning
26 between olivine and melt. We also calculated the mantle fO_2 on the basis of V/Sc ratios
27 of primary magmas of these intrusions.

28 Ni-Cu sulfide-bearing mafic-ultramafic intrusions in the CAOB include arc-related
29 Silurian-Carboniferous ones and post-collisional Permian-Triassic ones. Arc-related
30 intrusions formed before the closure of the paleo-Asian ocean and include the Jinbulake,
31 Heishan, Kuwei and Erbutu intrusions. Post-collisional intrusions were emplaced in
32 extensional settings after the closure of the paleo-Asian ocean and include the Kalatongke,
33 Baixintan, Huangshandong, Huangshan, Poyi, Poshi, Tulaergen and Hongqiling No.7
34 intrusions. It is clear that the magma fO_2 values of all these intrusions in both settings
35 range mostly from FMQ+0.5 to FMQ+3 and are generally elevated with the fractionation
36 of magmas, much higher than that of MORBs (FMQ-1 to FMQ+0.5). However, the
37 mantle fO_2 values of these intrusions vary from ~FMQ to ~FMQ+1.0, just slightly higher
38 than that of MORBs (\leq FMQ). This slight difference is interpreted as the intrusions in the
39 CAOB may have been derived from the metasomatized mantle wedges where only minor
40 slab-derived, oxidized components were involved. Therefore, the high magma fO_2 values

41 of most Ni-Cu sulfide-bearing mafic-ultramafic intrusions in the CAOBS were attributed
42 to the fractionation of magmas derived from the slightly oxidized metasomatized mantle.
43 In addition, the intrusions that host economic Ni-Cu sulfide deposits in the CAOBS usually
44 have magma fO_2 of $>FMQ+1.0$ and sulfides with mantle-like $\delta^{34}S$ values (-1.0 to +1.1‰),
45 indicating that the oxidized mafic magmas may be able to dissolve enough mantle-
46 derived sulfur to form economic Ni-Cu sulfide deposits. Oxidized mafic magmas derived
47 from metasomatized mantle sources may be an important feature of major orogenic belts.
48 *Keywords:* Mafic-ultramafic intrusion; Magmatic Ni-Cu sulfide mineralization; Magma
49 oxygen fugacity; Central Asian orogenic belt; Convergent margin setting

50

51

INTRODUCTION

52 The oxygen fugacity (fO_2) of mantle-derived mafic magmas is controlled by
53 equilibria of Fe^{3+} - Fe^{2+} and S^{2-} - S^{6+} (Kress and Carmichael, 1991; Jugo et al., 2005), and
54 can be quantified as $\Delta\log fO_2$ relative to mineral assemblage buffers. The fO_2 values of
55 mafic magmas are considered to be closely related to geodynamic settings, but how they
56 differ in different settings is still a matter of debate. In general, having $Fe^{3+}/\Sigma Fe$ and
57 $S^{6+}/\Sigma S$ higher than the mid-ocean ridge basalts (MORBs), arc and back-arc basalts may
58 have formed from relatively oxidized magmas (Wood et al., 1990; Nilsson and Peach,
59 1993; Jugo et al., 2010; Brounce et al., 2017). It has been demonstrated that arc and back-
60 arc basalts were derived from metasomatized mantle wedges that have been oxidized to
61 variable degrees (Debret et al., 2016; Rielli et al., 2017; Bénard et al., 2018). It is also
62 known that the metasomatized mantle beneath subduction zones has fO_2 similar to the
63 mantle beneath the mid-ocean ridges, and it is the fractionation of metasomatized mantle-

64 derived magmas or the interaction of hydrated magmas with ambient mantle that elevated
65 the magma fO_2 (Lee et al., 2005, 2010; Dauphas et al., 2010; Tollan and Hermann, 2019;
66 Li et al., 2020).

67 Magmatic Ni-Cu sulfide deposits are traditionally thought to be related to the mafic
68 magmatism induced by either mantle plumes or rifting within intraplate settings (Naldrett,
69 2004). However, mafic-ultramafic intrusions in convergent margin settings have become
70 targets for prospecting economic Ni-Cu sulfide deposits in recent years (Maier et al.,
71 2008; Thakurta et al., 2008; Tomkins et al., 2012; Manor et al., 2016; Song et al., 2016).
72 The mantle sources of such intrusions in are generally considered to be metasomatized by
73 slab-derived fluids/melts (Manor et al., 2016; Song et al., 2016). The mafic magmas
74 derived from the metasomatized mantle can be highly hydrated and oxidized with fO_2
75 being up to FMQ+6 (FMQ means fayalite-magnetite-quartz oxygen buffer) (Kelley and
76 Cottrell, 2009; Kelley et al., 2010; Gaillard et al., 2015). For example, the magma fO_2 of
77 the Alaskan-type Duke intrusion in USA and the Turnagain and Mascot Ni-Cu sulfide-
78 bearing mafic-ultramafic intrusions in Spain are calculated to be >FMQ+2 (Thakurta et
79 al., 2008; Manor et al., 2016). The central Asian orogenic belt (CAOB) is one of the
80 largest accretionary orogens in the world, resulted from large-scaled subduction and
81 accretion of juvenile materials from Neoproterozoic to Paleozoic (Sengör et al., 1993;
82 Xiao et al., 2004a, b, 2009; Jahn et al., 2004). A preliminary study on the oxidation states
83 of a few Ni-Cu sulfide-bearing mafic-ultramafic intrusions in the CAOB indicates that
84 magma fO_2 values vary from FMQ+0.3 to FMQ+2.6, much higher than that of MORBs
85 (Cao et al., 2019).

86 Experimental results indicate that the sulfur solubility of highly oxidized mafic
87 magmas can be as high as 1.4 wt.% with sulfur being dominantly as sulfate species (S^{6+})
88 (Jugo et al., 2005; Jugo, 2009), significantly higher than that of reduced mafic magmas
89 with dominantly S^{2-} phases (Jugo et al., 2010; Cottrell and Kelley, 2011). Therefore, the
90 oxidized mantle source or highly oxidized, hydrated mafic magmas may be more
91 favorable for the magmatic Ni-Cu sulfide deposits in convergent margin settings (Jenner
92 et al., 2010; Tomkins et al., 2012; Cao et al., 2019; Wei et al., 2019). However, the
93 linkage between magma fO_2 of mafic-ultramafic intrusions and Ni-Cu sulfide
94 mineralization is not well understood. Three important issues that should be answered: (1)
95 if the mantle sources of the mafic-ultramafic intrusions in convergent margin settings
96 have remarkably high fO_2 relative to those in intraplate settings? (2) if not, what triggers
97 high magma fO_2 of the mafic-ultramafic intrusions in convergent margin settings? and (3)
98 what is the favorable magma fO_2 for the Ni-Cu sulfide mineralization in convergent
99 margin settings?

100 A number of Paleozoic mafic-ultramafic intrusions in the CAOB host Ni-Cu sulfide
101 deposits with variable Ni grades and ore reserves, making up a ~4000-km-long Ni-Cu
102 sulfide mineralization belt in North China. These intrusions were dated to be Devonian to
103 Triassic in ages, some of which were emplaced in the subduction stage predating the
104 closure of the paleo-Asian ocean, whereas others in the post-subduction, extensional
105 stage after the closure of the paleo-Asian ocean (*e.g.*, Yang and Zhou, 2009; Qin et al.,
106 2011; Li et al., 2012; Yang et al., 2012; Peng et al., 2013; Li et al., 2015). These
107 intrusions are ideal to unravel the correlation between magma fO_2 and Ni-Cu sulfide
108 mineralization in a convergent margin setting. In this study, we estimated the mantle and

109 magma fO_2 of representative mafic-ultramafic intrusions in the CAOBS that were
110 emplaced in different ages and host variable degrees of Ni-Cu sulfide mineralization. The
111 results indicate that most intrusions have magma fO_2 much higher than that of MORBs
112 despite the similarity in their mantle fO_2 . Such a feature can be further examined for the
113 Ni-Cu sulfide-bearing mafic-ultramafic intrusions in convergent margin settings
114 elsewhere.

115

116 **GEOLOGICAL BACKGROUND**

117 The central Asian orogenic belt is bounded by the Siberian Craton to the north and
118 the Tarim Craton and North China Craton to the south (Fig. 1a). The belt extends for
119 more than 7000 km from the Pacific ocean to the Eastern Europe, making up one of the
120 largest accretionary orogenic belts on Earth. It formed due to the closure of the paleo-
121 Asian ocean in Paleozoic and comprises numerous fragments of Precambrian
122 microcontinents, Paleozoic island arcs, ophiolite suites, successions of volcanic rocks
123 (Windley et al., 2007; Xiao et al., 2009).

124 The CAOBS in China part is subdivided into the western and eastern segments (Zhou
125 and Wilde, 2013) (Fig. 1b). The western segment is further divided into five belts, from
126 north to south (Fig. 1c), including: 1) the Altay orogenic belt that is bounded by the
127 Sayan belt to the north and by the Ulungar fault and Junggar block to the south (Sengör et
128 al., 1993; Windley et al., 2002; Xiao et al., 2009), 2) the North Tianshan orogenic belt
129 between the Junggar block to the north and the Aqikkuduk fault to the south (Zhou et al.,
130 2004; Qin et al., 2011; Gao et al., 2012), 3) the Central Tianshan orogenic belt between
131 the Aqikkuduk fault to the north and the Kawabulak fault to the south (Song et al., 2013),

132 4) the South Tianshan orogenic belt between the Kawabulak fault to the north and the
133 Tarim Craton to the south (Yang and Zhou, 2009), and 5) the Beishan fold belt along the
134 northeastern margin of the Tarim Craton (Xu et al., 2016). The eastern segment refers to
135 the Xing'an-Mongolia orogenic belt in the Inner Mongolia and NE China (Zhang et al.,
136 2015), which consists mainly of, from north to south, the Erguna massif, Xing'an massif,
137 Songnen-Zhangguangcai range massif, and a continental margin accretionary belt (Wu et
138 al., 2007) (Fig. 1d).

139 Numerous mafic-ultramafic intrusions that contain Ni-Cu sulfide mineralization occur
140 in the CAOBS. They were emplaced mainly in two periods, one from Silurian to
141 Carboniferous and the other from Permian to Triassic (*e.g.*, Yang and Zhou, 2009; Xie et
142 al., 2012; Hao et al., 2014; Mao et al., 2016).

143 **Silurian to Carboniferous mafic-ultramafic intrusions**

144 Silurian to Carboniferous mafic-ultramafic intrusions are mainly distributed in the
145 western segment of the CAOBS and host small- to medium-sized Ni-Cu sulfide deposits
146 (Fig. 1b). As the paleo-Asian ocean was not yet closed until Permian in the western
147 segment (Han et al., 2007; Xiao et al., 2009), these intrusions are considered to be arc-
148 related (Yang and Zhou, 2009; Xie et al., 2012; Yang et al., 2012). Representative
149 intrusions include the Jinbulake intrusion (ca. 430 Ma) in the central Tianshan belt (Yang
150 and Zhou, 2009; Yang et al., 2012), the Kuwei intrusion (ca. 398 Ma) in the Altay belt
151 (Li et al., 2015), and the Heishan intrusion (ca. 356 to 367 Ma) in the Beishan belt (Xie et
152 al., 2012).

153 The parental magmas of these intrusions are tholeiitic (*e.g.*, Zhou et al., 2004; Yang
154 and Zhou, 2009; Tang et al., 2012; Xia et al., 2013; Song et al., 2013). Rocks of these

155 intrusions have positive $\varepsilon_{\text{Nd}}(t)$ (+0.4 to +4) and initial $\text{Sr}^{87}/\text{Sr}^{86}$ ranging from 0.704 to
156 0.709 (Yang and Zhou, 2009; Xie et al., 2012; Yang et al., 2012). They show depleted Nb
157 and Ta relative to large ion lithophile elements (LILE) and light rare earth elements
158 (LREE) on the primitive mantle-normalized trace element patterns (Fig. 2a-d), consistent
159 with an arc-like affinity. These features were interpreted as magma generation from the
160 depleted mantle that had been metasomatized by slab-derived fluids/melts (Yang and
161 Zhou, 2009; Xie et al., 2012; Yang et al., 2012).

162 The Erbutu intrusion in the eastern segment of the CAOB is an outlier. Although it is
163 dated to be 294.2 ± 2.7 Ma, it is considered to be an arc-hosted intrusion (Peng et al.,
164 2013). The intrusion hosts a small-sized Ni-Cu sulfide deposit and the parental magma is
165 boninitic (Peng et al., 2013). The intrusion is mainly composed of olivine-bearing
166 orthopyroxenite with mineral modes quite similar to those formed from boninitic magma
167 (Peng et al., 2013). The rocks have LREE and LILE (*e.g.*, Ba and Rb) more enriched than
168 those of the Jinbulake and Heishan intrusions (Fig. 2e, f).

169 **Permian to Triassic mafic-ultramafic intrusions**

170 Permian to Triassic mafic-ultramafic intrusions in the CAOB host a number of
171 economic Ni-Cu sulfide deposits, including the Kalatongke intrusion (290-282 Ma) in the
172 Altay belt (Song and Li, 2009; Zhang et al., 2009; Gao et al., 2012), the Huangshandong
173 and Huangshanxi intrusions (274-283 Ma) in the Huangshan-Jingerquan mineralized belt
174 in the North Tianshan belt (Qin et al., 2011; Sun et al., 2013), the Tulaergen intrusion
175 (265 ± 9.2 Ma) in the Kanggur-Huangshan shear zone in the North Tianshan belt (Zhao et
176 al., 2017), the Poyi and Poshi intrusions (270-277 Ma) in the Beishan belt (Xue et al.,
177 2016), and the Hongqiling No.7 and Piaohechuan No.4 intrusions (ca. 210-230 Ma) in the

178 Xing'an-Mongolia belt (Wei et al., 2013, 2015) (Fig. 1b). In addition, many other
179 intrusions in this period host potential Ni-Cu sulfide mineralization, including the
180 Huangshannan (278 ± 2 Ma) and Baixintan intrusions (286 ± 3 Ma) in the North Tianshan
181 belt (Mao et al., 2016; Feng et al., 2017), the Luodong intrusion (260-290 Ma) in the
182 Beishan belt (Su et al., 2015), and the Hongqiling No.1, 2, 3, 9, 32 and 33 intrusions (ca.
183 210-230 Ma) in the Xing'an-Mongolia belt (Hao et al., 2014).

184 These intrusions are considered to have formed in post-subduction, extensional
185 settings after the closure of the paleo-Asian ocean (*e.g.*, Jiang et al., 2009; Li et al., 2012;
186 Sun et al., 2013; Wei et al., 2013, 2015; Mao et al., 2014, 2015). The rocks of these
187 intrusions show arc-like trace element patterns (Fig. 3a-d), which are attributed to the
188 derivation from the metasomatized, depleted mantle (Xie et al., 2012; Li et al., 2012;
189 Mao et al., 2014; Deng et al., 2015). However, the rocks of the Luodong intrusion have
190 MORB-like, LREE-depleted trace element patterns (Fig. 3e, f), which may have been
191 derived from the weakly metasomatized mantle (Su et al., 2015).

192

193 **INTRUSIONS AND SAMPLES CHOSEN FOR OXYGEN FUGACITY**

194

CALCULATION

195 A prerequisite to use the olivine-spinel oxygen barometer is to obtain the
196 compositions of equilibrated olivine-spinel pair in rocks (Ballhaus et al., 1991). The
197 mafic-ultramafic intrusions in the CAOB that have rocks containing olivine-spinel pair
198 include Silurian to Carboniferous Jinbulake, Heishan and Erbutu intrusions, and Permian
199 to Triassic Baixintan, Huangshannan, Huangshandong, Huangshanxi, Poyi, Luodong,
200 Tulaergen, Hongqiling No.1 and No. 2 intrusions. In this study, we calculated the magma

201 and mantle fO_2 values of the Jinbulake, Heishan, Erbutu, Baixintan, Huangshannan,
202 Luodong, and Tulaergen intrusions. Together with the magma and/or mantle fO_2 values
203 of the Huangshandong, Huangshanxi, Poyi and Hongqiling No.1 and No. 2 intrusions that
204 were obtained in our earlier studies (Cao et al., 2019; Wei et al., 2019), an integrated
205 framework of the magma and mantle fO_2 of the Ni-Cu sulfide-bearing mafic-ultramafic
206 intrusions in the CAOBS can be outlined. The results in this study are compared with the
207 magma fO_2 values of the picrite in the Dali area, SW China, which is part of the
208 Emeishan large igneous province (LIP) that formed within an intraplate setting. The
209 petrography of the selected mafic-ultramafic intrusions in the CAOBS and the Dali picrite
210 in the Emeishan LIP were described in Supplementary Information.

211

212 ANALYTICAL RESULTS

213 Compositions of olivine-spinel pairs in mafic-ultramafic intrusions in the CAOBS

214 The compositions of the olivine-spinel pairs in the rocks of the selected mafic-
215 ultramafic intrusions in the CAOBS were analyzed in this study. Analytical methods were
216 described in Supplementary Information. The results of the olivine-spinel pairs are
217 described in Supplementary Information and the data are listed in Table S1.

218

219 A summary of spinel compositions

220 The spinel grains from the mafic-ultramafic intrusions in either arc or post-subduction,
221 extensional settings in the CAOBS have highly variable Cr# and XFe^{3+} . The grains from
222 the Erbutu intrusion have the highest Cr# and the lowest XFe^{3+} among the three arc-
223 hosted intrusions (Fig. 4a, b). Among the intrusions in the post-subduction, extensional

224 settings, the spinel grains from the Baixintan, Huangshannan and Tulaergen intrusions
225 have relatively restricted Cr# but highly variable XFe^{3+} relative to those from the
226 Luodong and Hongqiling No.1 and No.2 intrusions (Fig. 4a, b). In addition, the spinel
227 grains from the Luodong intrusion has similar Cr# but relatively low and restricted XFe^{3+}
228 compared to those from the Hongqiling No.1 and No.2 intrusions (Fig. 4a, b). The spinel
229 grains from the Erbutu and Luodong intrusions are clustered on the plot of Mg# versus
230 XFe^{3+} , whereas the grains from each of other intrusions generally show a negative trend
231 of Mg# versus XFe^{3+} on this plot (Fig. 4b).

232 The spinel grains in the Dali picrite overall have higher Mg# and Cr#, and lower
233 XFe^{3+} than those from the intrusions in the CAO B (Fig. 4a, b). However, they have
234 similar Cr# and XFe^{3+} to those from the Erbutu intrusion (Fig. 4a, b). They display a
235 nearly horizontal trend on the plot of Mg# versus XFe^{3+} (Fig. 4b), which is in contrast to
236 the negative correlation trend for the spinel from the intrusions in the CAO B on the plot.

237

238 **S isotope compositions of sulfides in mafic-ultramafic intrusions in the CAO B**

239 The method of *in situ* S isotope analysis for the sulfides (pyrrhotite, pentlandite and
240 chalcopyrite) in the rocks of the selected mafic-ultramafic intrusions in the CAO B is
241 described in Supplementary Information. The sulfides in the wehrlite of the Jinbulake
242 intrusion have $\delta^{34}S$ ranging from +0.3 to +1.3‰ (Table 1). The sulfides in the lherzolite
243 of the Baixintan intrusion have $\delta^{34}S$ ranging from -0.7 to +1.2‰ (Table 1). The sulfides
244 in the lherzolite of the Tulaergen intrusion have $\delta^{34}S$ ranging from -0.2 to +0.8‰ (Table
245 1). Overall, the sulfides from the three intrusions have a restricted range of $\delta^{34}S$ from -0.7
246 to +1.3‰. Likewise, the sulfides in the ores of three economic Ni-Cu sulfide deposits

247 hosted in the Permian-Triassic Kalatongke, Hongqiling No. 7 and Piaohechuan No. 4
248 intrusions in the CAO B have $\delta^{34}\text{S}$ ranging from -1.0 to +1.1‰ (Wei et al., 2019). All of
249 these values are similar to the $\delta^{34}\text{S}$ of MORB-type mantle (-1.5 to +0.6‰, Labidi et al.,
250 2013, 2014) (Fig. 5). In contrast, the sulfides from the rocks of the Erbutu intrusion have
251 $\delta^{34}\text{S}$ ranging from +5.3 to +7.5‰ (Table 1), much higher than those from other intrusions
252 in the CAO B (Fig. 5).

253

254 **CALCULATION RESULTS OF OXYGEN FUGACITY**

255 The oxygen fugacity of the mantle and mantle-derived mafic magmas can be
256 calculated in four different ways, including: 1) measuring $\text{Fe}^{3+}/(\text{Fe}^{3+}+\text{Fe}^{2+})$ of basalts or
257 quenched basaltic glass (Kress and Carmichael, 1991; Kelley and Cottrell, 2009), 2)
258 quantifying the partition coefficients of redox-sensitive elements (*e.g.*, V and Cr) in the
259 differentiation of magma (Canil, 1997; Mallmann and O'Neill, 2009), 3) using oxygen
260 barometers based on the chemical equilibria between mineral pairs (*e.g.*, olivine-spinel
261 pair) (Ballhaus et al., 1991), and 4) calculating the ratios of redox sensitive/insensitive
262 elements (*e.g.*, V/Sc, Fe^1/Zn) of primary magmas (Lee et al., 2005, 2010; Mallmann and
263 O'Neill, 2009). The fourth method is exclusively used to estimate the mantle oxygen
264 fugacity (Lee et al., 2005; Mallmann and O'Neill, 2009), however, the three others are
265 applicable to calculate the $f\text{O}_2$ of both mantle and mantle-derived magmas, depending on
266 that the examined objects are mantle xenoliths (*e.g.*, Ionov and Wood, 1992), or
267 fractionated basalts/mafic-ultramafic intrusions (*e.g.*, Cao et al., 2019).

268 **Mantle $f\text{O}_2$**

269 Given that the mantle xenolith that can be directly used to calculate the mantle fO_2 are
270 unavailable in the CAOB, we constrained the mantle fO_2 based on the relationship
271 between the mantle fO_2 and the V/Sc ratios of primary magmas, an alternative method
272 proposed by Lee et al. (2005) and Mallmann and O'Neill (2009). Because V is sensitive
273 to redox and Sc is not, the V/Sc ratio of primary magma is mainly governed by fO_2
274 during partial melting of a given mantle lithology (Lee et al., 2005; Mallmann and
275 O'Neill, 2009), and is not affected by temperature and pressure (Canil and Fedortchouk,
276 2000; Li, 2018). In addition, the V/Sc ratio of basaltic magma is not sensitive to the
277 crystallization of olivine (Lee et al., 2005; Mallmann and O'Neill, 2009), the V/Sc ratio
278 of the melt in equilibrium with the most primitive olivine in a mafic-ultramafic intrusion
279 can be taken as the ratio of primary magma, particularly if olivine is the only cumulus
280 phase. Therefore, we selected the samples from the Heishan, Huangshannan, Luodong,
281 Poyi and Hongqiling No.2 intrusions in the CAOB that contain high Fo olivine (Fo = 86
282 to 90) as the only cumulus phase, the obtained V/Sc ratio of the melt in equilibrium with
283 the olivine is analog to the V/Sc ratio of the primary magma of the intrusion.

284 As olivine is the only cumulus phase in the rocks, the concentrations of V and Sc of
285 the melt can be calculated using the mass balance equation (Godel et al., 2011):

$$286 \quad C_{WR}^{V,Sc} = F_{Ol} \times C_{Ol}^{V,Sc} + (1-F_{Ol}) \times C_{Liq}^{V,Sc} \quad (1)$$

287 where $C_{WR}^{V,Sc}$ and $C_{Ol}^{V,Sc}$ is the concentrations of V and Sc in the bulk rock and cumulus
288 olivine, respectively. The fraction of olivine (F_{Ol}) can be estimated in two ways; one is to
289 analyze the back-scattered electron (BSE) images or scan thin sections of the samples, the
290 other is to use the mass balance of whole-rock MgO and FeO contents combined with the
291 olivine-liquid exchange coefficient (Kd) (Li and Ripley, 2011). In this study, we

292 integrated the two ways to obtain the F_{O_1} and then calculated the concentrations of V and
293 Sc in the melt ($C_{Liq}^{V, Sc}$) based on equation (1) (Table S2).

294 The V/Sc ratios of primary magmas would increase slightly with the degrees of
295 partial melting of the mantle at a given mantle fO_2 when it is \leq FMQ, but would decrease
296 significantly when it is $>$ FMQ (Lee et al., 2005) (Fig. 6). Therefore, the degrees of partial
297 melting of the mantle should be considered when the V/Sc ratio of primary magma is
298 used to calculate mantle fO_2 . Mafic magmas in subduction zones are generally produced
299 by higher degrees of partial melting of the mantle (e.g., up to 15-20%, Kelley et al., 2006)
300 than those in the mid-ocean ridges (~10%, Bottinga and Allegre, 1976). The degrees of
301 partial melting of the mantle are thus set to be 15 to 20% for the intrusions in the CAO, B,
302 the obtained mantle fO_2 of the Heishan, Huangshannan, Luodong, Poyi and Hongqiling
303 No.2 intrusions is \sim FMQ+1.0, \sim FMQ, \sim FMQ, \sim FMQ+1.0 and \sim FMQ+0.5, respectively
304 (Fig. 6).

305 In our previous study, the mantle fO_2 of the Poyi and Hongqiling No.2 intrusions was
306 estimated to be FMQ+0.3 and FMQ+0.5, respectively, using the olivine-spinel oxygen
307 barometer (Cao et al., 2019). As the chemical data of the spinel from the Poyi intrusion in
308 that study were collected from the literature and the $Fe^{3+}/\Sigma Fe$ of the spinel was not
309 corrected, the obtained mantle fO_2 was likely underestimated by \sim 0.6 log unit (Cao et al.,
310 2019), so the mantle fO_2 of the Poyi intrusion could be \sim FMQ+0.9. Therefore, the mantle
311 fO_2 of the Poyi and Hongqiling No.2 intrusions obtained by two different ways are quite
312 consistent with each other.

313 **Magma fO_2**

314 The magma fO_2 of the mafic-ultramafic intrusions in the CAO B was acquired by two
315 methods; one is based on the olivine-spinel oxygen barometer (Ballhaus et al., 1991), the
316 other is based on V partitioning in olivine (Canil, 1997; Shishkina et al., 2018).

317 **Olivine-spinel oxygen barometer.** The oxygen fugacity of magmas was calculated
318 using the olivine-spinel oxygen barometer given by Ballhaus et al. (1991):

$$\begin{aligned} 319 \log_{10} fO_2 (\Delta QFM) = & 0.27 + 2505/T - 400P/T - 6\log(X_{Fe}^{Ol}) - 3200(1 - X_{Fe}^{Ol})^2/T + \\ 320 & 2\log(X_{Fe^{2+}}^{Spl}) + 4\log(X_{Fe^{3+}}^{Spl}) + 2630(X_{Al}^{Spl})^2/T \quad (2) \end{aligned}$$

321 where P is pressure in GPa, T is temperature in K, X_{Fe}^{Ol} is molar $Fe^{2+}/(Fe^{2+}+Mg^{2+})$ in
322 olivine, $X_{Fe^{3+}}^{Spl}$ is molar $Fe^{3+}/\Sigma R^{3+}$ in spinel, X_{Al}^{Spl} is molar Al/ ΣR^{3+} in spinel, and $X_{Fe^{2+}}^{Spl}$ is
323 molar $Fe^{2+}/(Fe^{2+}+Mg^{2+})$ in spinel. Olivine grains in the samples from the intrusions in the
324 CAO B have Fo contents varying from 82 to 90, with most being >84 (Table S1), and
325 those from the Dali picrite have Fo contents varying from 82 to 92 (Kamenetsky et al.,
326 2012; Liu et al., 2017), which are all applicable to the equation. The pressure was
327 calculated using the clinopyroxene geobarometer given by Nimis and Ulmer (1998)
328 (Table S1). The $Fe^{3+}/\Sigma Fe$ of the spinel from the Jinbulake, Erbutu, Baixintan,
329 Huangshannan and Tulaergen intrusions is corrected based on the EPMA data obtained in
330 this study, whereas the $Fe^{3+}/\Sigma Fe$ of the spinel from the Heishan, Luodong intrusions and
331 Dali picrite cannot be corrected as the EPMA data were collected from the literature. The
332 magma fO_2 calculated using uncorrected $Fe^{3+}/\Sigma Fe$ of the spinel is 0.2 to 0.6 log units
333 lower than that using corrected $Fe^{3+}/\Sigma Fe$ (Cao et al., 2019). However, the bias becomes
334 smaller with increasing fO_2 , which is <0.4 log units when fO_2 is >FMQ+1, and is <0.2 log
335 units when fO_2 is >FMQ+1.5 (Cao et al., 2019).

336 The accuracy of the results depends on whether or not the olivine-spinel pairs in the
337 rocks are in chemical equilibrium (Ballhaus et al., 1991). The spinel grains in this study
338 overall are euhedral, fresh and homogeneous, and are commonly enclosed within olivine
339 (Fig. S1c). The textures showing chemical disequilibrium, such as complex zoning,
340 embayment, symplectite and sieve texture, are not observed in both minerals. In addition,
341 the olivine-spinel pairs in the rocks from the intrusions in the CAOB overall have
342 $\ln K_{\text{Mg/Fe}}^{\text{Ol-Spl}}$ positively correlated with $X_{\text{Cr}^{3+}}$ [molar $\text{Cr}^{3+}/(\text{Fe}^{3+}+\text{Cr}^{3+}+\text{Al}^{3+})$] along the
343 equilibrium lines between 600 and 700°C (Fig. 7), indicating that the olivine-spinel pairs
344 reached chemical equilibrium. The temperatures of the equilibrium lines on Fig. 7 were
345 estimated from the experimental data related to the reciprocal reaction (FeCr_2O_4
346 $+\text{MgAl}_2\text{O}_4 = \text{MgCr}_2\text{O}_4 + \text{FeAl}_2\text{O}_4$) in spinel (Liermann and Ganguly, 2003), which are
347 consistent with the equilibrium temperatures calculated using the olivine-spinel
348 thermometer given by Ballhaus et al. (1991) (Table S1). It is noted that the obtained
349 temperature values are the closure temperatures of Mg-Fe²⁺ diffusion between olivine
350 and spinel on subsolidus cooling, which are lower than the crystallization temperature of
351 minerals (Kamenetsky et al., 2001). However, the $f\text{O}_2$ could be only elevated by ~0.2 log
352 units due to subsolidus Mg-Fe²⁺ equilibrium between the olivine-spinel pairs (Birner et
353 al., 2018). Therefore, the $f\text{O}_2$ values obtained using the closure temperatures of the
354 olivine-spinel pairs can be taken as the magma $f\text{O}_2$ of the intrusions.

355 Using the equation 2, we obtained the magma $f\text{O}_2$ of the Jinbulake, Heishan, Erbutu,
356 Baixintan, Huangshannan, Luodong and Tulaergen intrusions, which ranges from
357 FMQ+1.2 to FMQ+2.6, FMQ+1.3 to FMQ+2.3, FMQ-0.1 to FMQ+1.2, FMQ+1.3 to
358 FMQ+3.0, FMQ+0.6 to FMQ+2.6, FMQ+0.3 to FMQ+1.7, FMQ+2.5 to FMQ+2.9,

359 respectively (Table S1 and Fig. 8a). Although the values for the Heishan and Luodong
360 intrusions were calculated using uncorrected $\text{Fe}^{3+}/\Sigma\text{Fe}$ of the spinel, the upper values
361 should be reliable (*c.f.*, Cao et al., 2019). These data, together with the magma $f\text{O}_2$ of the
362 Huangshandong, Huangshanxi, Poyi and Hongqiling No.1 and No.2 intrusions obtained
363 in our earlier studies (Cao et al., 2019; Wei et al., 2019), display a negative correlation
364 between the magma $f\text{O}_2$ and the Fo contents of olivine, except for the Erbutu intrusion
365 (Fig. 8b).

366 The olivine-spinel pairs from the Dali picrite plot between the equilibrium lines at
367 900 and 1100°C (Fig. 7). The magma $f\text{O}_2$ of the Dali picrite varies from FMQ+0.2 to
368 FMQ+0.8 (Fig. 8a). Given that the uncorrected $\text{Fe}^{3+}/\Sigma\text{Fe}$ of the spinel was used in the
369 calculation, the results could be underestimated by ~ 0.6 log units in this case (*c.f.*, Cao et
370 al., 2019). However, even if the bias is considered, the magma $f\text{O}_2$ of the Dali picrite is
371 still much lower than the magma $f\text{O}_2$ of the mafic-ultramafic intrusions in the CAOB (Fig.
372 8a).

373 **Vanadium partitioning in olivine (D_V^{Ol}).** Experimental results demonstrated that the
374 partition coefficient of V between olivine and melt will decrease with elevating magma
375 $f\text{O}_2$ (*e.g.*, Canil, 1997, 2002; Mallmann and O'Neill, 2013; Laubier et al., 2014; Shishkina
376 et al., 2018). This relationship was used to calculate the magma $f\text{O}_2$ of hydrous arc basalts
377 (Shishkina et al., 2018), *i.e.*,

$$378 \quad \Delta\text{FMQ} = -3.07 \times \log D_V^{Ol} - 3.34 \quad (3)$$

379 A common way to measure D_V^{Ol} is to acquire the V concentration of melt inclusion
380 and host olivine in basalts. However, melt inclusions trapped in the olivine of cumulates

381 are difficult to be found and analyzed as they are usually very small. We therefore chose
382 an alternative protocol to estimate the D_v^{Ol} .

383 Vanadium and Sc are highly incompatible to olivine and have similar diffusion rates
384 between olivine and trapped liquid in crystal mush (Locmelis et al., 2019), the V/Sc ratio
385 of olivine is thus hardly affected by the trapped liquid shift effect. In addition, the V/Sc
386 ratio of olivine is resistant to post-magmatic overprints, crustal contamination and
387 crystallization of small amounts of spinel (<5%) (Lee et al., 2005; Locmelis et al., 2019).
388 Nevertheless, we tried to analyze the core part of the best-preserved olivine grains in each
389 sample to warrant that the primary V/Sc ratio of olivine is acquired. In theory, the V/Sc
390 ratio of olivine can be calculated using the equation:

$$391 \quad \left(\frac{V}{Sc}\right)_{Ol} = \frac{D_v^{Ol} \times V_{Liq}}{D_{Sc}^{Ol} \times Sc_{Liq}} \quad (4)$$

392 Since D_{Sc}^{Ol} is constant at ~0.2 (Villemant et al., 1981; Sun and Liang, 2013), the
393 equation 4 can be simplified as the equation:

$$394 \quad \left(\frac{V}{Sc}\right)_{Ol} = \frac{D_v^{Ol} \times V_{Liq}}{0.2 \times Sc_{Liq}} \quad (5)$$

395 D_v^{Ol} can be then acquired through the equation:

$$396 \quad D_v^{Ol} = 0.2 \times \frac{\left(\frac{V}{Sc}\right)_{Ol}}{\left(\frac{V}{Sc}\right)_{Liq}} \quad (6)$$

397 If equation 6 is combined with equation 3, the magma fO_2 can be calculated by the
398 equation:

$$399 \quad \Delta FMQ = -3.07 \times \log \left[0.2 \times \frac{\left(\frac{V}{Sc}\right)_{Ol}}{\left(\frac{V}{Sc}\right)_{Liq}} \right] - 3.34 \quad (7)$$

400 Although V and Sc are highly incompatible to both olivine and orthopyroxene, Sc is
401 more compatible to clinopyroxene than V (Canil, 2002). $(V/Sc)_{Liq}$ would vary slightly
402 when olivine and/or orthopyroxene are on liquidus, but increase significantly when
403 clinopyroxene is on liquidus during the fractionation of mafic magmas (Laubier et al.,
404 2014). Most samples in this study contain olivine and/or orthopyroxene as major cumulus
405 minerals (Fig. S1), except for those from the Jinbulake intrusion. Therefore, $(V/Sc)_{Liq}$ can
406 be referred to the V/Sc ratio of the primary magma for each intrusion in the CAO
407 (Table S2), and then the magma fO_2 of the intrusions can be directly calculated using
408 equation 7 (Table S3).

409 **Comparison of the results based on the two methods.** The obtained magma fO_2
410 values based on the two methods are consistent with each other within uncertainties (Fig.
411 9a). The V/Sc ratios of the olivine from the Erbutu, Huangshannan, Hongqiling No.1 and
412 No.2 intrusions generally decrease with increasing magma fO_2 values that were obtained
413 based on the olivine-spinel oxygen barometer (Fig. 9b), indicating that the obtained
414 magma fO_2 values in this study is reliable (*c.f.*, Canil, 1997, 2002; Mallmann and O'Neill,
415 2013; Laubier et al., 2014; Shishkina et al., 2018).

416 In summary, the magma fO_2 values of the arc-hosted Jinbulake and Heishan
417 intrusions are comparable to those of the post-collisional Baixintan, Huangshandong,
418 Huangshanxi, Huangshannan, Tulaergen, Hongqiling No.1 and No.2 intrusions. The
419 magma fO_2 values of the mafic-ultramafic intrusions in the CAO overall have a range
420 similar to those of arc basalts (FMQ+0.5 to FMQ+6; Woodland et al., 2006), much
421 higher than those of MORBs (FMQ-1 to FMQ+0.5; Cottrell and Kelley, 2011; Zhang et
422 al., 2018) (Fig. 8a). The magma fO_2 values of the Erbutu, Poyi and Luodong intrusions

423 are lower than that of other intrusions in the CAOBS, and overlap the upper fO_2 limit of
424 MORBs (Fig. 8a). In contrast, the magma fO_2 values of the Dali picrite are basically
425 within the range of MORBs (Fig. 8a).

426

427

DISCUSSIONS

428 The magma fO_2 of mafic-ultramafic intrusions in convergent margin settings could be
429 controlled by complex factors such as the oxidation and fertility states of the
430 metasomatized mantle sources (*e.g.*, Rielli et al., 2017), and magmatic processes (*e.g.*,
431 Lee et al., 2005). In this study, our results indicate that metasomatized mantle sources of
432 the mafic-ultramafic intrusions in the CAOBS overall are slightly oxidized compared with
433 that of MORBs, and the elevated magma fO_2 of the intrusions in both arc and post-
434 subduction, extensional settings is mainly attributed to the fractionation of hydrated
435 magmas derived from the metasomatized mantle.

436 **Mantle fO_2 of the mafic-ultramafic intrusions in the CAOBS**

437 The arc-related Heishan intrusion and post-collisional Huangshannan, Poyi, Luodong
438 and Hongqiling No.2 intrusions have mantle fO_2 ranging from ~FMQ to ~FMQ+1.0 (Fig.
439 6), slightly higher than the mantle fO_2 (\leq FMQ) of MORBs (Frost and McCammon, 2008;
440 Kelley and Cottrell, 2009, 2012; Rielli et al., 2018a), but much lower than the mantle fO_2
441 of arc basalts (FMQ+1 to FMQ+4, Woodland et al., 2006). These results indicate that the
442 mantle sources of mafic-ultramafic intrusions in the CAOBS are not highly oxidized as
443 supposed for the subarc mantle. In addition, the mantle fO_2 is much lower than the
444 magma fO_2 of these intrusions (Fig. 8b), the high magma fO_2 of the intrusions in the
445 CAOBS is thus not governed by the oxidation state of the mantle source alone.

446 The oxidation of the subarc mantle is attributed to the transportation of highly
447 oxidized, CO_3^{2-} , SO_4^{2-} , or Fe^{3+} -rich fluids to the subarc mantle during subduction
448 (Mungall, 2002; Evans, 2006; Evans et al., 2012; Debret et al., 2016; Pons et al., 2016;
449 Debret and Sverjensky, 2017; Rielli et al., 2017). However, this process is dependent on
450 the subduction depth and temperature (Tomkins and Evans, 2015). Modeling results
451 indicate that sulfate tends to be released at shallower subduction zone and relatively low
452 temperatures, whereas sulfide tends to be released at deeper subduction zone and
453 relatively high temperatures (Tomkins and Evans, 2015). The mafic-ultramafic intrusions
454 in the CAOB are considered to have been derived from partial melts of the mantle wedge
455 in the spinel stability field (*e.g.*, Zhang et al., 2016). It is likely that only minor slab-
456 derived, oxidized components was involved in the mantle wedge at this depth. In addition,
457 the mantle sources of these intrusions in the CAOB are considered to have experienced
458 the interaction of the depleted lithospheric mantle with upwelling asthenospheric
459 materials due to slab break-off (Han et al., 2010; Li et al., 2012; Xie et al., 2012; Wei et
460 al., 2013; Mao et al., 2014, 2016; Deng et al., 2015). This process may also dilute the
461 oxidized components in the mantle wedge because asthenospheric materials are typically
462 more reduced than the lithospheric mantle by ~ 1 log unit (Wood et al., 1990). Therefore,
463 the mafic-ultramafic intrusions in the CAOB overall have mantle $f\text{O}_2$ slightly higher than
464 that for the mantle of MORBs.

465 **Fractionation of hydrated magmas derived from metasomatized mantle sources**

466 Experimental results indicate that the fractionation of olivine and clinopyroxene may
467 slightly increase the $\text{Fe}^{3+}/\sum\text{Fe}$ of magmas and have a limited effect on the oxidization
468 states of magmas (Cottrell and Kelley, 2011; Kelley and Cottrell, 2012). However, water

469 in silicate magmas can play an efficient ‘catalyst’ to promote the oxidation states of
470 magmas if it is partially dissociated and loss H^+ at high temperatures (Carmichael, 1991;
471 Cornejo and Mahood, 1997), or exsolved from the melt that carried more Fe^{2+} than Fe^{3+}
472 (Bell and Simon, 2011). Mafic magmas tend to become more hydrous with fractionation
473 because volatiles (*e.g.*, H_2O) are essentially incompatible to olivine and clinopyroxene.
474 Therefore, the fractionation process could significantly elevate the oxidation states of
475 hydrated, mafic magmas.

476 The mafic-ultramafic intrusions in the CAOB contain abundant hydrous minerals
477 such as amphibole and phlogopite (*e.g.*, Deng et al., 2014; Su et al., 2011; Xie et al., 2012;
478 Wei et al., 2013, 2015). On the plot of Al_z versus TiO₂, the clinopyroxene from the
479 intrusions in the CAOB has Al_z/Ti scattered along the arc cumulate trend, in contrast to
480 the low Al_z/Ti of the clinopyroxene from the sulfide-bearing mafic-ultramafic intrusions
481 in the Emeishan LIP (Fig. 10). The high Al_z values of the clinopyroxene from the CAOB
482 are attributed to the idea that more Al would enter the tetrahedral site of clinopyroxene
483 with increasing H_2O content of melt (*c.f.*, Loucks, 1990). This is consistent with an
484 interpretation that the parental magmas of the intrusions in the CAOB may be hydrated
485 due to the derivation from the mantle sources metasomatized by slab-derived melts/fluids.
486 There is an overall negative correlation between the magma fO_2 and the Fo contents of
487 olivine for the intrusions in the CAOB (Fig. 8b), showing that the magmas became more
488 oxidized with fractionation. Therefore, the H_2O content of magmas derived from the
489 metasomatized mantle and relative degrees of the fractionation of magmas are likely two
490 key factors controlling magma fO_2 of the mafic-ultramafic intrusions in convergent
491 margin settings.

492 The Erbutu intrusion is an exceptional case as the olivine grains of the intrusion have
493 Fo contents comparable with those for the olivine of the Jinbulake and Heishan intrusions,
494 but the intrusion has much lower magma fO_2 than the latter two intrusions (Fig. 8b). The
495 parental magma of the Erbutu intrusion is thought to be boninitic that may have been
496 emplaced early in the subduction history (*c.f.*, Jian et al., 2010; Peng et al., 2013). As the
497 oxidation of the mantle wedge by the metasomatizing agents could occur after subduction
498 initiation in 1 Myr. (*c.f.*, Brounce et al., 2015), it is likely that the mantle source of the
499 Erbutu intrusion is relatively reduced, thus the magma fO_2 of this intrusion is lower than
500 that of other intrusions in the CAOB for a given degree of fractionation of magma.

501

502 **Magma fO_2 constraints for Ni-Cu sulfide mineralization in convergent margin** 503 **settings**

504 Experimental results show that the sulfur solubility of silicate magma could increase
505 by an order of magnitude if the magma fO_2 increases from FMQ+0.5 to FMQ+1.5 (Luhr,
506 1990; Jugo et al., 2005; Jugo, 2009; Jugo et al., 2010). The mantle-derived mafic magmas
507 in intraplate settings usually have magma fO_2 ranging from FMQ-1 to FMQ+0.5 and
508 could dissolve a maximum of ~1500 ppm S (*c.f.*, Wood et al., 1990; Jugo et al., 2010),
509 therefore the formation of economic Ni-Cu sulfide deposits often requires the addition of
510 external crustal sulfur into the magmas (*e.g.*, Li et al., 2001; Ripley and Li, 2003; Barnes
511 and Lightfoot, 2005; Wang et al., 2006; Mungall and Naldrett, 2008; Keays and Lightfoot,
512 2010; Taranovic et al., 2018). For instance, the Ni-Cu sulfide deposits in the Emeishan
513 LIP and the Jinchuan Ni-Cu deposit formed in a rifting setting have magma fO_2
514 overlapping with the range of MORBs, and the sulfides from the deposits have highly

515 variable $\delta^{34}\text{S}$ (-4 to +8‰, Fig. 11), indicating substantial addition of external crustal
516 sulfur in the formation of these deposits (Ripley et al., 2005; Duan et al., 2016; Wang et
517 al., 2018).

518 In contrast, the mantle-derived mafic magmas in convergent margin settings have $f\text{O}_2$
519 ranging from FMQ+0.5 to FMQ+3 (Fig. 8a) and could dissolve ~1800 to ~13,000 ppm S
520 (Jugo et al., 2010), much higher than the S solubility of the magmas in intraplate settings.
521 In addition, the sulfides from the Ni-Cu sulfide-bearing mafic-ultramafic intrusions in the
522 post-subduction, extensional setting in the CAOB have $\delta^{34}\text{S}$ values (-1.0 to +1.3‰)
523 nearly identical to that of the MORB mantle (Fig. 11), despite the large $\delta^{34}\text{S}$ range (-10.0
524 to +5.4‰) of the sulfides from the metasomatized mantle xenoliths (Rielli et al., 2018b).
525 This was interpreted as the magmas of the Ni-Cu sulfide-bearing mafic-ultramafic
526 intrusions in the CAOB contain dominantly mantle-derived sulfur with trivial addition of
527 external crustal sulfur (Wei et al., 2019). Therefore, the high magma $f\text{O}_2$ and the MORB
528 mantle-like $\delta^{34}\text{S}$ of the mafic-ultramafic intrusion in the CAOB indicate that highly
529 oxidized, mantle-derived magmas may be capable of dissolving enough mantle-derived
530 sulfur to form magmatic Ni-Cu sulfide deposits so that the addition of external crustal
531 sulfur is not always necessary in such cases. In addition, the mafic-ultramafic intrusions
532 in the CAOB that have sulfides with mantle-like $\delta^{34}\text{S}$ values generally have magma
533 $f\text{O}_2 > \text{FMQ}+1$, whereas the Erbutu intrusion that has sulfides with the highest $\delta^{34}\text{S}$ values
534 has magma $f\text{O}_2 < \text{FMQ}+1$ (Fig. 11), we thus consider that the mantle-derived mafic
535 magmas with $f\text{O}_2$ greater than ~FMQ+1.0 may be able to dissolve sufficient mantle-
536 derived sulfur to form important Ni-Cu sulfide deposits in convergent margin settings
537 (*c.f.*, Rielli et al., 2018a).

538 On the other hand, the formation of economic Ni-Cu sulfide deposits from the highly
539 oxidized, mantle-derived magmas depends on how the magmas can be reduced to reach
540 sulfide saturation so that the sulfide melts can be segregated from the magmas (Tomkins
541 et al., 2012). This can be examined by comparing the fO_2 between the parental magmas
542 prior to sulfide saturation and the magmas concurrent with sulfide saturation (*e.g.*, Wei et
543 al., 2019). The magma fO_2 obtained by the olivine-spinel oxygen barometer in this study
544 can represent the parental magma fO_2 before sulfide saturation. The fO_2 of the magmas
545 concurrent with sulfide saturation for the intrusions in the CAOB were estimated using
546 Fe-Ni exchange between olivine and sulfide liquid (*e.g.*, Feng et al., 2017; Mao et al.,
547 2018; Wei et al., 2019). As shown in Fig. 12, the magma fO_2 at sulfide saturation is
548 considerably lower than the fO_2 of parental magmas for each intrusion, indicating that the
549 oxidized magmas was indeed reduced with the sulfide saturation of magmas. A possible
550 way to trigger the reduction is the crystallization of magnetite (Jenner et al., 2010).
551 However, this mechanism does not appear as the driver of magma reduction in the CAOB
552 because the examined rocks in this study contain few magnetite. Alternatively, the
553 reduction of oxidized magmas can be triggered by the addition of organic-carbon or
554 graphite-rich sedimentary rocks, which was evidenced by the C isotope studies on a few
555 intrusions in the CAOB (*e.g.*, Wei et al., 2019) and the O isotope studies of the olivine in
556 the lower zone of the Huangshanxi intrusion (Mao et al., 2019).

557

558

IMPLICATIONS

559 Most Ni-Cu sulfide-bearing mafic-ultramafic intrusions in the CAOB have magma
560 fO_2 (FMQ+0.5 to FMQ+3) much higher than that of MORBs (FMQ-1 to FMQ+0.5),

561 consistent with the global observation that the mafic-ultramafic intrusions emplaced in
562 convergent margin settings have relatively high magma fO_2 . In contrast, the mantle fO_2 of
563 these intrusions ranges from FMQ to \sim FMQ+1.0, just slightly higher than that of MORBs
564 (\leq FMQ). Because the amounts of oxidized components that were added to the
565 metasomatized mantle wedges generally decrease with the depth of the mantle wedges in
566 convergent margin settings, the slightly oxidized mantle source of the intrusions in the
567 CAOB is likely related to the limited amounts of slab-derived, oxidized components
568 added to mantle wedges and relatively deep mantle wedges where the partial melting
569 occurred. The negative correlation of the magma fO_2 and the Fo contents of the olivine of
570 the intrusions in the CAOB indicates that the magma fO_2 could be elevated with the
571 fractionation of hydrated, mafic magmas derived from metasomatized mantle sources. In
572 addition, the mafic-ultramafic intrusions that host economic Ni-Cu sulfide deposits in the
573 CAOB usually have sulfides with mantle-like $\delta^{34}S$ (-1.0 to +1.1‰) and magma
574 $fO_2 > FMQ + 1$, indicating that the relatively oxidized magmas may be capable of
575 dissolving enough mantle-derived sulfur to form economic Ni-Cu sulfide deposits in
576 convergent margin settings. The sulfide saturation of the oxidized, mafic magmas may be
577 triggered by the addition of organic-carbon or graphite-rich sedimentary rocks into the
578 magmas. Therefore, our results imply that the addition of external crustal sulfur is not so
579 compulsory to trigger the sulfide saturation of highly oxidized, mantle-derived mafic
580 magmas and the formation of economic Ni-Cu sulfide deposits in convergent margin
581 settings, although it is very important in the formation of giant Ni-Cu sulfide deposits
582 such as those at Noril'sk in Russia (Ripley and Li, 2013).
583

584

ACKNOWLEDGEMENTS AND FUNDING

585 This work was supported by grants from the National Natural Science Foundation of
586 China (No. 41730423 and 41902077), and China Postdoctoral Science Foundation Grant
587 (No. 2019M653103). Shenghong Yang provided the samples of the Jinbulake intrusion
588 and Benxun Su shared the EPMA data for the olivine and spinel of the Luodong intrusion.
589 Constructive reviews by Andrew Tomkins and an anonymous reviewer have greatly
590 improved the quality of this manuscript.

591

592

REFERENCES

- 593 Ballhaus C., Berry R.F., and Green D.H. (1991) High pressure experimental calibration
594 of the olivine-orthopyroxene-spinel oxygen geobarometer: implications for the
595 oxidation state of the upper mantle. *Contributions to Mineralogy and Petrology* 107,
596 27–40.
- 597 Barnes S.-J., and Lightfoot P.C. (2005) Formation of magmatic nickel-sulfide ore
598 deposits and processes affecting their copper and platinum-group element contents.
599 In *Economic Geology 100th Anniversary Volume* (eds. J. W. Hedenquist, J. H.
600 Thompson, R. J. Goldfarb and J. P. Richards). pp. 179-213.
- 601 Bell A.S., and Simon A. (2011) Experimental evidence for the alteration of the $\text{Fe}^{3+}/\Sigma\text{Fe}$
602 of silicate melt caused by the degassing of chlorine-bearing aqueous volatiles.
603 *Geology* 39, 499–502.
- 604 Bénard A., Woodland A.B., Arculus R.J., Nebel O., and McAlpine S.R.B. (2018)
605 Variation in sub-arc mantle oxygen fugacity during partial melting recorded in
606 refractory peridotite xenoliths from the West Bismarck Arc. *Chemical Geology* 486,
607 16–30.
- 608 Birner A., Cottrell E., Warren J.M., Kelley K.A., Davis F.A. (2018) Peridotites and
609 basalts reveal broad congruence between two independent records of mantle $f\text{O}_2$
610 despite local redox heterogeneity. *Earth and Planetary Science Letters* 494, 172-189.
- 611 Bottinga Y., and Allegre C. (1976). Geophysical, petrological and geochemical models of
612 the oceanic lithosphere. *Tectonophysics* 32, 9–59.

27

- 613 Brounce M., Kelley K.A., Cottrell E. and Reagan M.K. (2015) Temporal evolution of
614 mantle wedge oxygen fugacity during subduction initiation. *Geology* 43, 775–778.
- 615 Brounce M., Stolper E., and Eiler J. (2017) Redox variations in Mauna Kea lavas, the
616 oxygen fugacity of the Hawaiian plume, and the role of volcanic gases in Earth’s
617 oxygenation. *PNAS* 114, 8997–9002.
- 618 Canil D. (1997) Vanadium partitioning and the oxidation state of Archean komatiite
619 magmas. *Nature* 389, 842–845.
- 620 Canil D. (2002) Vanadium in peridotites, mantle redox and tectonic environments:
621 Archean to present. *Earth and Planetary Science Letters* 195, 75–90.
- 622 Canil D., and Fedortchouk Y. (2001) Olivine-liquid partitioning of vanadium and other
623 trace elements, with applications to modern and ancient picrites. *The Canadian*
624 *Mineralogist* 39, 319–330.
- 625 Cao Y., Wang C.Y., and Wei B. (2019) Magma oxygen fugacity of Permian to Triassic
626 Ni-Cu sulfide-bearing mafic-ultramafic intrusions in the central Asian orogenic belt,
627 North China. *Journal of Asian Earth Sciences* 173, 250–262.
- 628 Carmichael I.S.E. (1991) The redox states of basic and silicic magmas- a reflection of
629 their source regions. *Contributions to Mineralogy and Petrology* 106, 129–141.
- 630 Cornejo P.C., and Mahood G.A. (1997) Seeing past the effects of re-equilibration to
631 reconstruct magmatic gradients in plutons: La Gloria Pluton, central Chilean Andes.
632 *Contributions to Mineralogy and Petrology* 127, 159–175.
- 633 Cottrell E., and Kelley K.A. (2011) The oxidation state of Fe in MORB glasses and the
634 oxygen fugacity of the upper mantle. *Earth and Planetary Science Letters* 305, 270–
635 282.
- 636 Dauphas N., Teng F.-Z., and Arndt N.T. (2010) Magnesium and iron isotopes in 2.7 Ga
637 Alexo komatiites: Mantle signatures, no evidence for Soret diffusion, and
638 identification of diffusive transport in zoned olivine. *Geochimica et Cosmochimica*
639 *Acta* 74, 3274–3291.
- 640 Debret B., and Sverjensky D.A. (2017) Highly oxidising fluids generated during
641 serpentinite breakdown in subduction zones. *Scientific Report* 1–6.
- 642 Debret B., Millet M.-A., Pons M.-L., Bouilhol P., Inglis E., and Williams H. (2016)
643 Isotopic evidence for iron mobility during subduction. *Geology* 44, 215–218.

- 644 Deng Y.F., Song X.Y., Chen L., Zhou T., Pirajno F., Yuan F., Xie W., and Zhang D.
645 (2014) Geochemistry of the Huangshandong Ni-Cu deposit in northwestern China:
646 Implications for the formation of magmatic sulfide mineralization in orogenic belts.
647 Ore Geology Reviews 56, 181–198.
- 648 Deng Y.F., Song X.Y., Hollings P., Zhou T.F., Yuan F., and Zhang D. (2015) Role of
649 asthenosphere and lithosphere in the genesis of the Early Permian Huangshan mafic-
650 ultramafic intrusion in the Northern Tianshan, NW China. Lithos 227, 241–254.
- 651 Duan J., Li C., Qian Z., Jiao J., Ripley E.M., and Feng Y. (2016) Multiple S isotopes,
652 zircon Hf isotopes, whole-rock Sr-Nd isotopes, and spatial variations of PGE tenors
653 in the Jinchuan Ni-Cu-PGE deposit, NW China. Mineralium Deposita 51, 557–574.
- 654 Evans B.W., Dyar M.D., and Kuehner S.M. (2012) Implications of ferrous and ferric iron
655 in antigorite. American Mineralogist 97, 184–196.
- 656 Evans K.A. (2006) Redox decoupling and redox budgets: Conceptual tools for the study
657 of earth systems. Geology 34, 489-492.
- 658 Feng Y., Qian Z., Xu G., Duan J., Chen B., Sun T., Jiang C., and Ren M. (2017) Rock-
659 forming mineral features of Permian mineralized mafic-ultramafic intrusions in East
660 Tianshan Mountains and their implications for intrusion generation. Acta
661 Petrological et Mineralogical 36, 519-534 (in Chinese with English abstract).
- 662 Frost D.J., and McCammon C.A. (2008) The redox state of earth's mantle. Annual
663 Review of Earth and Planetary Science 389-420.
- 664 Gaillard F., Scaillet B., Pichavant M., and Lacono-Marziano G. (2015) The redox
665 geodynamics linking basalts and their mantle sources through space and time.
666 Chemical Geology 418, 217–233.
- 667 Gao J.-F., Zhou M.-F., Lightfoot P., and Qu W. (2012) Heterogeneous Os isotope
668 compositions in the Kalatongke sulfide deposit, NW China: the role of crustal
669 contamination. Mineralium Deposita 47, 731–738.
- 670 Godel B., Barnes S.J., and Maier W. D. (2011) Parental magma composition inferred
671 from trace element in cumulus and intercumulus silicate minerals: an example from
672 the lower and lower critical zones of the Bushveld Complex, South-Africa. Lithos
673 125, 537–552.

- 674 Han C., Xiao W., Zhao G., Ao S., Zhang J., Qu W., and Du A. (2010) In-situ U-Pb, Hf
675 and Re-Os isotopic analyses of the Xiangshan Ni-Cu- Co deposit in Eastern
676 Tianshan (Xinjiang), Central Asia Orogenic Belt: Constraints on the timing and
677 genesis of the mineralization. *Lithos* 120, 547–562.
- 678 Han C., Xiao W., Zhao G., Qu W., and Du A. (2007) Re–Os dating of the Kalatongke
679 Cu–Ni deposit, Altay Shan, NW China, and resulting geodynamic implications. *Ore
680 Geology Reviews* 32, 452–468.
- 681 Hao L., Zhao X., Boorder H.D., Lu J., Zhao, Y., and Wei, Q. (2014) Origin of PGE
682 depletion of Triassic magmatic Cu-Ni sulfide deposits in the central-southern area of
683 Jilin province, NE China. *Ore Geology Reviews* 63, 226–237.
- 684 Ionov D.A., and Wood B.J. (1992) The oxidation state of subcontinental mantle: oxygen
685 thermobarometry of mantle xenoliths from central Asia. *Contributions to
686 Mineralogy and Petrology* 111, 179–193.
- 687 Jahn B.M., Windley B., Natal'in B., and Dobretsov N. (2004) Phanerozoic continental
688 growth in Central Asia. *Journal of Asian Earth Sciences* 23, 599-603.
- 689 Jahn B.M., Wu F.Y., and Chen B. (2000) Massive granitoid generation in Central Asia:
690 Nd isotope evidence and implication for continental growth in the Phanerozoic.
691 *Episodes* 23, 82–92.
- 692 Jenner F.E., O'Neill H.St.C., Arculus R.J., and Mavrogenes J.A. (2010) The magnetite
693 crisis in the evolution of arc-related magmas and the initial concentration of Au, Ag
694 and Cu. *Journal of Petrology* 51, 2445–2464.
- 695 Jian P., Liu D., Kröner A., Windley B.F., Shi Y., Zhang W., Zhang F., Miao L., Zhang L.,
696 and Tomurhuu D. (2010) Evolution of a Permian intraoceanic arc–trench system in
697 the Solonker suture zone, Central Asian Orogenic Belt, China and Mongolia. *Lithos*
698 118, 169-190.
- 699 Jiang Y.-H., Jiang S.-Y., Dai B.-Z., Liao S.-Y., Zhao K.-D., and Ling H.-F. (2009)
700 Middle to late Jurassic felsic and mafic magmatism in southern Hunan Province,
701 southeast China: Implications for a continental arc to rifting. *Lithos* 107, 185–204.
- 702 Jugo P.J. (2009) Sulfur content at sulfide saturation in oxidized magmas. *Geology* 37,
703 415–418.

- 704 Jugo P.J., Luth R.W., and Richards J.P. (2005) Experimental data on the speciation of
705 sulfur as a function of oxygen fugacity in basaltic melts. *Geochimica et*
706 *Cosmochimica Acta* 69, 497–503.
- 707 Jugo P.J., Wilke M., and Botcharnikov R.E. (2010) Sulfur K-edge XANES analysis of
708 natural and synthetic basaltic glasses: Implications for S speciation and S content as
709 function of oxygen fugacity. *Geochimica et Cosmochimica Acta* 74, 5926–5938.
- 710 Kamenetsky V.S., Chung S.-L., Kamenetsky M.B., and Kuzmin D.V. (2012) Picrites
711 from the Emeishan large igneous province, SW China: a compositional continuum
712 in primitive magmas and their respective mantle sources. *Journal of Petrology* 53,
713 2095-2113.
- 714 Kamenetsky V.S., Crawford A.J., and Meffre S. (2001) Factors controlling chemistry of
715 magmatic spinel: An empirical study of associated olivine, Cr-spinel and melt in-
716 clusions from primitive rocks. *Journal of Petrology* 42, 655–671.
- 717 Keays R.R., and Lightfoot P.C. (2010) Crustal sulfur is required to form magmatic Ni–Cu
718 sulphide deposits; evidence from chalcophile element signatures of Siberian and
719 Deccan Trap basalts. *Mineralium Deposita* 45, 241–257
- 720 Kelley K.A., and Cottrell E. (2009) Water and the oxidation state of Subduction Zone
721 Magmas. *Science* 325, 605–607.
- 722 Kelley K.A., and Cottrell E. (2012) The influence of magmatic differentiation on the
723 oxidation state of Fe in a basaltic arc magma. *Earth and Planetary Science Letters*
724 329–330, 109–121.
- 725 Kelley K.A., Plank T., Grove T.L., Stolper E.M., Newman S., and Hauri E. (2006).
726 Mantle melting as a function of water content beneath back-arc basins. *Journal of*
727 *Geophysical Research: Solid Earth* 111, B09208.
- 728 Kelley K.A., Plank T., Newman S., Stolper E., Grove T.L., Parman S., and Hauri E.
729 (2010) Mantle melting as a function of water content beneath the Mariana arc.
730 *Journal of Petrology* 51, 1711–1738.
- 731 Kress V.C., and Carmichael I.S.E. (1991) The compressibility of silicate liquids
732 containing Fe₂O₃ and the effect of composition, temperature, oxygen fugacity and
733 pressure on their redox states. *Contributions to Mineralogy and Petrology* 108, 82–92

- 734 Labidi J., Cartigny P., and Moreira M. (2013) Non-chondritic sulphur isotope
735 composition of the terrestrial mantle. *Nature* 501, 208–211.
- 736 Labidi J., Cartigny P., Hamelin C., Moreira M., and Dosso L. (2014) Sulfur isotope
737 budget (^{32}S , ^{33}S , ^{34}S and ^{36}S) in Pacific-Antarctic Ridge basalts; a record of mantle
738 source heterogeneity and hydrothermal sulfide assimilation. *Geochimica et*
739 *Cosmochimica Acta* 133, 47–67.
- 740 Laubier M., Grove T.L., and Langmuir C.H. (2014) Trace element mineral/melt
741 partitioning for basaltic and basaltic andesitic melts: An experimental and laser ICP-
742 MS study with application to the oxidation state of mantle source regions. *Earth and*
743 *Planetary Science Letters* 392, 265–278.
- 744 Lee C.T.A., Leeman W.P., Canil D., and Li Z.X.A. (2005) Similar V/Sc systematics in
745 MORB and arc basalts: Implications for the oxygen fugacities of their mantle source
746 regions. *Journal of Petrology* 46, 2313–2336.
- 747 Lee C.T.A., Luffi P., Le Roux V., Dasgupta R., Albarède F., and Leeman W.P. (2010)
748 The redox state of arc mantle using Zn/Fe systematics. *Nature* 468, 681–685.
- 749 Li C., and Ripley E.M. (2011) The giant Jinchuan Ni-Cu-(PGE) deposit; tectonic setting,
750 magma evolution, ore genesis, and exploration implications. *Reviews in Economic*
751 *Geology* 17, 163–180.
- 752 Li C., Maier W.D., and Waal S.A. (2001) Magmatic Ni-Cu versus PGE deposits:
753 contrasting genetic controls and exploration implication. *South African Journal of*
754 *Geology* 104, 205–214.
- 755 Li C., Zhang M.J., Fu P., Qian Z.Z., Hu P.Q., and Ripley E.M. (2012) The Kalatongke
756 magmatic Ni-Cu deposits in the Central Asian Orogenic Belt, NW China: product of
757 slab window magmatism? *Mineralium Deposita* 47, 51–67.
- 758 Li C., Zhang Z., Li W., Wang Y., Sun T., and Ripley E.M. (2015) Geochronology,
759 petrology and Hf-S isotope geochemistry of the newly-discovered Xiarihamu
760 magmatic Ni-Cu sulfide deposit in the Qinghai-Tibet plateau, western China. *Lithos*
761 216, 224–240.
- 762 Li J.L., Schwarzenbach E.M., John T., Ague J.J., Huang F., Gao, J., Klemd R.,
763 Whitehouse M.J., and Wang X.S. (2020) Uncovering and quantifying the subduction
764 zone sulfur cycle from the slab perspective. *Nature Communications* 11, 1-12.

- 765 Li Y. (2018) Temperature and pressure effects on the partitioning of V and Sc between
766 clinopyroxene and silicate melt: Implications for mantle oxygen fugacity. American
767 Mineralogist 103, 819–823.
- 768 Liermann H.P., and Ganguly J. (2003) Fe²⁺-Mg fractionation between orthopyroxene and
769 spinel: experimental calibration in the system FeO–MgO–Al₂O₃–Cr₂O₃–SiO₂, and
770 applications. Contributions to Mineralogy and Petrology 154, 217–227.
- 771 Liu J., Xia Q.-K., Kuritani T., Hanski E., and Yu H.-R. (2017) Mantle hydration and the
772 role of water in the generation of large igneous provinces. Nature Communication 8,
773 1824.
- 774 Locmelis M., Arevalo R.D., Puchtel I.S., Fiorentini M.L., and Nisbet E.G. (2019)
775 Transition metals in komatiitic olivine: Proxies for mantle composition, redox
776 conditions, and sulfide mineralization potential. American Mineralogist 104, 1143–
777 1155.
- 778 Loucks R.R. (1990) Discrimination from ophiolitic and nonophiolitic ultramafic–mafic
779 allochthons in orogenic belts by the Al/Ti ratios in clinopyroxene. Geology 18, 346–
780 349.
- 781 Luhr J.F. (1990) Experimental phase relations of water- and sulfur-saturated arc magmas
782 and the 1982 eruptions of El Chichon volcano. Journal of Petrology 31, 1071–1114.
- 783 Maier W.D., Barnes S.J., Chinyepi G., Barton J.J., Eglington B., and Setshedi T. (2008)
784 The composition of magmatic Ni-Cu-(PGE) sulfide deposits in the Tati and Selebi-
785 Phikwe belts of eastern Botswana. Mineralium Deposita 43, 37-60.
- 786 Mallmann G., and O'Neill H.S.C. (2009) The crystal/melt partitioning of V during
787 mantle melting as a function of oxygen fugacity compared with some other elements
788 (Al, P, Ca, Sc, Ti, Cr, Fe, Ga, Y, Zr and Nb). Journal of Petrology 50, 1765–1794.
- 789 Mallmann G., and O'Neill H.S.C. (2013) Calibration of an empirical thermometer and
790 oxybarometer based on the partitioning of Sc, Y and V between olivine and silicate
791 melt. Journal of Petrology 54, 933–949.
- 792 Manor M.J., Scoates J.S., Nixon G.T., and Ames D.E. (2016) The giant mascot Ni-Cu-
793 PGE deposit, British Columbia: mineralized conduits in a convergent margin
794 tectonic setting. Economic Geology 111, 57–87.

- 795 Mao Y., Qin K., Barnes S. J., Ferraina C., Iacono–Marziano G., Verrall M., Tang D., and
796 Xue S. (2018) A revised oxygen barometry in sulfide-saturated magmas and
797 application to the Permian magmatic Ni–Cu deposits in the southern Central Asian
798 Orogenic Belt. *Mineralium Deposita* 53, 731–755.
- 799 Mao Y., Qin K., Li C., and Tang D. (2015) A modified genetic model for the
800 Huangshandong magmatic sulfide deposit in the Central Asian Orogenic Belt,
801 Xinjiang, western China. *Mineralium Deposita* 50, 65–82.
- 802 Mao Y., Qin K., Li C., Xue S., and Ripley E.M. (2014) Petrogenesis and ore genesis of
803 the Permian Huangshanxi sulfide ore-bearing mafic-ultramafic intrusion in the
804 Central Asian Orogenic Belt, western China. *Lithos* 200–201, 111–125.
- 805 Mao Y., Qin K., Tang D., Feng H. and Xue S. (2016) Crustal contamination and sulfide
806 immiscibility history of the Permian Huangshannan magmatic Ni-Cu sulfide deposit,
807 East Tianshan, NW China. *Journal of Asian Earth Sciences* 129, 22–37.
- 808 Mao Y.J., Barnes S.J., Qin K.Z., Tang D., Martin L., Su B., and Evans N.J. (2019) Rapid
809 orthopyroxene growth induced by silica assimilation: constraints from sector-zoned
810 orthopyroxene, olivine oxygen isotopes and trace element variations in the
811 Huangshanxi Ni–Cu deposit, Northwest China. *Contributions to Mineralogy and
812 Petrology* 174, 1–24.
- 813 Mungall J. E. (2002) Roasting the mantle: Slab melting and the genesis of major Au and
814 Au-rich Cu deposits. *Geology* 30, 915–918.
- 815 Mungall J.E., and Naldrett A.J. (2008) Ore Deposits of the Platinum-Group Elements.
816 *Element* 4, 253–258.
- 817 Naldrett A.J. (2004) Magmatic sulfide deposits: geology, geochemistry and exploration.
818 Springer, New York.
- 819 Nilsson K., and Peach C.L. (1993) Sulfur speciation, oxidation state and sulfur
820 concentration in backarc magmas. *Geochimica et Cosmochimica Acta* 57, 3807–
821 3813.
- 822 Nimis P., and Ulmer P. (1998) Clinopyroxene geobarometry of magmatic rocks Part 1:
823 An expanded structural geobarometer for anhydrous and hydrous, basic and
824 ultrabasic systems. *Contributions to Mineralogy and Petrology* 133, 122–135.

- 825 Peng R., Zhai Y., Li C., and Ripley M. (2013) The Erbutu Ni-Cu deposit in the Central
826 Asian Orogenic Belt: A Permian Magmatic Sulfide deposit related to boninitic
827 magmatism in an arc setting. *Economic Geology* 108, 1879-1888.
- 828 Pons M.-L., Debret B., Bouilhol P., Delacour A., and Williams H. (2016) Zinc isotope
829 evidence for sulfate-rich fluid transfer across subduction zones. *Nature*
830 *Communication* 7, 13794.
- 831 Qin K.Z., Su B.X., Li X.H., Tang D.M., Sakyi P.A., Sun H., Xiao Q.H., and Liu P.P.
832 (2011). SIMS zircon U-Pb geochronology and Sr-Nd isotopes of mafic-ultramafic
833 intrusions in eastern Tianshan and Beishan in correlation with flood basalts in Tarim
834 basin (NW China): Constraints on a 280 Ma mantle plume. *American Journal of*
835 *Sciences* 29, 275–289.
- 836 Rielli A., Tomkins A.G., Nebel O., Brugger J., Etschmann B., and Paterson D. (2018a)
837 Garnet peridotites reveal spatial and temporal changes in the oxidation potential of
838 subduction. *Scientific Reports* 8, 16411.
- 839 Rielli A., Tomkins A.G., Nebel O., Brugger J., Etschmann B., Zhong R., Yaxley G.M.,
840 and Paterson D. (2017) Evidence of sub-arc mantle oxidation by sulphur and carbon.
841 *Geochemical Perspective Letters* 124–132.
- 842 Rielli A., Tomkins A.G., Nebel O., Raveggi M., Jeon H., Martin L., and Ávila J.N.
843 (2018b) Sulfur isotope and PGE systematics of metasomatised mantle wedge. *Earth*
844 *and Planetary Science Letters* 497, 181–192.
- 845 Ripley E.M., and Li C. (2003) Sulfur isotope exchange and metal enrichment in the
846 formation of magmatic Cu-Ni-(PGE) deposits. *Economic Geology* 99, 635–641.
- 847 Ripley E.M., and Li, C. (2013) Sulfide saturation in mafic magmas: Is external sulfur
848 required for magmatic Ni-Cu-(PGE) ore genesis? *Economic Geology* 108, 45-58.
- 849 Ripley E.M., Sarkar A., and Li C. (2005) Mineralogical and stable isotope studies of
850 hydrothermal alteration at the Jinchuan Ni-Cu deposit. *Economic Geology* 100,
851 1349–1361.
- 852 Sengör A.C.A., Natal'in B.A., and Burtmann V.S. (1993) Evolution of the Altaid tectonic
853 collage and Palaeozoic crustal growth in Eurasia. *Nature* 364, 299–306.
- 854 Shishkina T.A., Portnyagin M.V., Botcharnikov R.E., Almeev R.R., Simonyan A.V.,
855 Garbe-Schönberg D., Schuth S., Oeser M., and Holtz F. (2018) Experimental

- 856 Calibration and Implications of Olivine-Melt Vanadium Oxybarometry for Hydrous
857 Basaltic Arc Magmas. *American Mineralogist* 103, 369–383.
- 858 Song X.-Y., and Li X.-R. (2009) Geochemistry of the Kalatongke Ni-Cu- (PGE) sulfide
859 deposit, NW China: Implications for the formation of magmatic sulfide
860 mineralization in a postcollisional environment. *Mineralium Deposita* 44, 303–327.
- 861 Song X.-Y., Chen L.-M., Deng Y.-F., and Xie W. (2013) Syncollisional tholeiitic
862 magmatism induced by asthenosphere upwelling owing to slab detachment at the
863 southern margin of the Central Asian orogenic belt. *Journal of Geological Society*
864 170, 941–950.
- 865 Song X.-Y., Yi J., Chen L., She Y., Liu C., Dang X.F., Yang Q., and Wu S. (2016) The
866 Giant Xiarihamu Ni-Co sulfide deposit in the East Kunlun Orogenic Belt, Northern
867 Tibet Plateau. China. *Economic Geology* 111, 29–55.
- 868 Su B.X., Qin K.Z., Lu Y., Sun H., and Sakyi P.A. (2015) Decoupling of whole-rock Nd-
869 Hf and zircon Hf-O isotopic compositions of a 284 Ma mafic-ultramafic intrusion in
870 the Beishan Terrane, NW China. *International Journal of Earth Sciences* 104, 1721-
871 1737.
- 872 Su B.X., Qin K.Z., Sakyi P.A., Li X.H., Yang Y.H., Sun H., Tang D.M., Liu P.P., Xiao
873 Q.H., and Malaviarachchi S.P.K. (2011) U–Pb ages and Hf-O isotopes of zircons
874 from Late Paleozoic mafic–ultramafic units in the southern Central Asian Orogenic
875 Belt: tectonic implications and evidence for an Early-Permian mantle plume.
876 *Gondwana Research* 20, 516–531.
- 877 Sun C., and Liang Y. (2013) The importance of crystal chemistry on REE partitioning
878 between mantle minerals (garnet, clinopyroxene, orthopyroxene, and olivine) and
879 basaltic melts. *Chemical Geology* 358, 23–36.
- 880 Sun S.S., and McDonough W.F. (1989) Chemical and isotopic systematics of oceanic
881 basalts: implications for mantle composition and processes. *Geological Society,*
882 London, Special Publications 42, 313–345.
- 883 Sun T., Qian Z.-Z., Li C., Xia M.-Z., and Yang S.-H. (2013) Petrogenesis and economic
884 potential of the Erhongwa mafic-ultramafic intrusion in the Central Asian Orogenic
885 Belt, NW China: Constraints from olivine chemistry, U-Pb age and Hf isotopes of
886 zircons, and whole-rock Sr-Nd-Pb isotopes. *Lithos* 182–183, 185–199.

- 887 Tang D., Qin K., Sun H., Su B., and Xiao Q. (2012) The role of crustal contamination in
888 the formation of Ni-Cu sulfide deposits in Eastern Tianshan, Xinjiang, Northwest
889 China: Evidence from trace element geochemistry, Re-Os, Sr-Nd, zircon Hf- O, and
890 sulfur isotopes. *Journal of Asian Earth Sciences* 49, 145–160.
- 891 Taranovic V., Ripley E. M., Li C. and Shirey, S.B. (2018) S, O, and Re-Os isotope
892 studies of the Tamarack Igneous Complex: melt-rock interaction during the early
893 stage of Midcontinent Rift Development. *Economic Geology* 113, 1161–1179.
- 894 Thakurta J., Ripley E.M., and Li, C. (2008) Geochemical constraints on the origin of
895 sulfide mineralization in the Duke Island Complex, southeastern Alaska.
896 *Geochemistry, Geophysics, Geosystems* 9, 1–34.
- 897 Tollan P., and Hermann J. (2019). Arc magmas oxidized by water dissociation and
898 hydrogen incorporation in orthopyroxene. *Nature Geoscience* 12, 667–671.
- 899 Tomkins A.G., and Evans K.A. (2015) Separate zones of sulfate and sulfide release from
900 subducted mafic oceanic crust. *Earth and Planetary Science Letters* 428, 73–83.
- 901 Tomkins A.G., Rebryna K.C., Weinberg R.F., and Schaefer B.F. (2012) Magmatic
902 sulfide formation by reduction of oxidized arc basalt. *Journal of Petrology* 53, 1537–
903 1567.
- 904 Villemant B., Jaffrezic H., Joron J.L., and Treuil M. (1981) Distribution coefficients of
905 major and trace-elements-fractional crystallization in the alkali basalt series of
906 Chaine- Des-Puys (Massif Central, France). *Geochimica et Cosmochimica Acta* 45,
907 1997–2016.
- 908 Wang C.Y., Wei B., Zhou M., Minh Huu D., and Qi, L. (2018) A synthesis of magmatic
909 Ni-Cu- (PGE) sulfide deposits in the ~ 260 Ma Emeishan large igneous province,
910 SW China and northern Vietnam. *Journal of Asian Earth Sciences* 154, 162–186.
- 911 Wang C.Y., Zhou M.F., and Keays, R.R. (2006) Geochemical constraints on the origin of
912 the Permian Baimazhai mafic-ultramafic intrusion, SW China. *Contributions to
913 Mineralogy and Petrology* 152, 309–321.
- 914 Wang R.M., Liu D.Q., and Yin D.T. (1987) The conditions of controlling metallogeny of
915 Cu-Ni sulfide ore deposits and the orientation of finding ore Hami, Xinjiang, China.
916 *Journal of Mineralogy and Petrology* 7, 1–152.

- 917 Wang Y.L. (2011) Petrogenesis and mineralization of Heishan intrusion in Beishan area,
918 Gansu. M.Sc. thesis, Chang'an University.
- 919 Wei B. (2013) Platinum-group element and Re-Os isotopic compositions of the magmatic
920 Ni-Cu sulfide deposits in the Hongqiling-Chajianling-Piaohechuan region, eastern
921 part of the Central Asian Orogenic Belt. Ph. D. thesis, University of Chinese
922 Academy of Sciences.
- 923 Wei B., Wang C.Y., Arndt N.T., Prichard H.M., and Fisher P.C. (2015) Textural
924 relationship of sulfide Ores, PGE, and Sr-Nd-Os isotope compositions of the
925 Triassic Piaohechuan Ni-Cu sulfide deposit in NE China. *Economic Geology* 110,
926 2041–2062.
- 927 Wei B., Wang C.Y., Lahaye Y., Xie L., and Cao Y. (2019) S and C Isotope Constraints
928 for Mantle-Derived Sulfur Source and Organic Carbon-Induced Sulfide Saturation
929 of Magmatic Ni-Cu Sulfide Deposits in the Central Asian Orogenic Belt, North
930 China. *Economic Geology* 114, 787–806.
- 931 Wei B., Wang C.Y., Li C., and Sun Y. (2013) Origin of PGE-depleted Ni-Cu sulfide
932 mineralization in the Triassic Hongqiling No. 7 orthopyroxenite intrusion, Central
933 Asian Orogenic Belt, northeastern China. *Economic Geology* 108, 1813–1831.
- 934 Windley B.F., Alexeiev D., Xiao W., Kröner A., and Badarch G. (2007) Tectonic models
935 for accretion of the Central Asian Orogenic Belt. *Journal of Geological Society* 164,
936 31–47.
- 937 Windley B.F., Kröner A., Guo J., Qu G., Li Y., and Zhang C. (2002) Neoproterozoic to
938 Paleozoic geology of the Altai orogen, NW China: new zircon age data and tectonic
939 evolution. *Journal of Geology* 110, 719–737.
- 940 Wood B.J., Bryndzia L.T., and Johnson K.E. (1990) Mantle oxidation state and its
941 relationship to tectonic environment and fluid speciation. *Science* 248, 337–345.
- 942 Woodland A.B., Kornprobst J., and Tabit A. (2006) Ferric iron in orogenic lherzolite
943 massifs and controls of oxygen fugacity in the upper mantle. *Lithos* 89, 222–241.
- 944 Wu F.Y., Zhao G.C., Sun D.Y., Wilde S.A., and Yang J.H. (2007) The Hulan Group: Its
945 role in the evolution of the Central Asian Orogenic Belt of NE China. *Journal of*
946 *Asian Earth Sciences* 30, 542–556.

- 947 Xia M.-Z., Jiang C.-Y., Li C., and Xia Z.-D. (2013) Characteristics of a newly discovered
948 Ni-Cu sulfide deposit hosted in the Poyi ultramafic intrusion, Tarim Craton, NW
949 China. *Economic Geology* 108, 1865–1878.
- 950 Xiao W.J., Windley B.F., Badarch G., Sun S., Li J.L., Qin K.Z., and Wang Z.H. (2004a)
951 Palaeozoic accretionary and convergent tectonics of the southern Altaids:
952 implications for the lateral growth of Central Asia. *Journal of Geological Society*,
953 London 161, 339-342.
- 954 Xiao W.J., Windley B.F., Huang B.C., Han C.M., Yuan C., Chen H.L., Sun M., Sun S.,
955 and Li J.L. (2009) End-Permian to mid-Triassic termination of the accretionary
956 processes of the southern Altaids: implications for the geodynamic evolution,
957 Phanerozoic continental growth, and metallogeny of Central Asia. *International*
958 *Journal of Earth Sciences* 98, 1189-1287.
- 959 Xiao W.J., Zhang L.C., Qin K.Z., Sun S., and Li J.L. (2004b) Paleozoic accretionary and
960 collisional tectonics of the Eastern Tianshan (China): implications for the
961 continental growth of central Asia. *American Journal of Sciences* 304, 370-395.
- 962 Xie W, Song X.Y., Chen L.M., Deng Y.F., Zheng W.Q., Wang Y.S., Ba D.H., Zhang
963 X.Q., and Luan Y. (2014) Geochemistry insights on the genesis of the subduction-
964 related Heishan magmatic Ni-Cu-(PGE) deposit in Gansu, NW China, at the
965 southern margin of the Central Asian Orogenic Belt. *Economic Geology* 109, 1563–
966 1583.
- 967 Xie W., Song X., Deng Y., Wang Y., and Ba D. (2012) Geochemistry and petrogenetic
968 implications of a Late Devonian mafic- ultramafic intrusion at the southern margin
969 of the Central Asian Orogenic Belt. *Lithos* 144–145, 209–230.
- 970 Xu X., Song S.G., Allen M.B., Ernst R.E., Niu Y.L., and Su L. (2016) An 850–820 Ma
971 LIP dismembered during breakup of the Rodinia supercontinent and destroyed by
972 Early Paleozoic continental subduction in the northern Tibetan Plateau, NW China.
973 *Precambrian Research* 282, 52–73.
- 974 Xu Y., Chung S., Jahn B., and Wu G. (2001) Petrologic and geochemical constraints on
975 the petrogenesis of Permian- Triassic Emeishan flood basalts in southwestern China.
976 *Lithos* 58, 145-168.

- 977 Xue S.C., Qin K.Z., Li C., Tang D.M., Mao Y.J., Qi L., and Ripley E.M. (2016)
978 Geochronological, petrological, and geochemical constraints on Ni-Cu sulfide mi-
979 neralization in the Poyi ultramafic-troctolitic intrusion in the northeast rim of the
980 Tarim Craton, Western China. *Economic Geology* 111, 1465–1484.
- 981 Yang S.H., and Zhou M.F. (2009) Geochemistry of the ~ 430-Ma Jingbulake mafic-
982 ultramafic intrusion in Western Xinjiang, NW China: implications for subduction
983 related magmatism in the South Tianshan orogenic belt. *Lithos* 113, 259–273.
- 984 Yang S.H., Zhou M.F., Lightfoot P.C., Malpas J., Qu W.J., Zhou J.B., and Kong D.Y
985 (2012) Selective crustal contamination and decoupling of lithophile and chalcophile
986 element isotopes in sulfide-bearing mafic intrusions: an example from the
987 Jingbulake intrusion, Xinjiang, NW China. *Chemical Geology* 302, 106–118.
- 988 Zhang H.L., Cottrell E., Solheid P.A., Kelley K.A., and Hirschmann M.M. (2018)
989 Determination of $\text{Fe}^{3+}/\Sigma\text{Fe}$ of XANES basaltic glass standards by Mössbauer
990 spectroscopy and its application to the oxidation state of iron in MORB. *Chemical*
991 *Geology* 479, 166–175.
- 992 Zhang X., Zhao G., Eizenhöfer P.R., Sun M., Han Y., Hou W., Liu D., Wang B., Liu Q.,
993 Xu B., and Yanlin C. (2016) Tectonic transition from Late Carboniferous subduction
994 to Early Permian post-collisional extension in the Eastern Tianshan, NW China:
995 Insights from geochronology and geochemistry of mafic-intermediate intrusions.
996 *Lithos* 257, 269–281.
- 997 Zhang Z., Li K., Li J., Tang W., Chen Y., and Luo Z. (2015) Geochronology and
998 geochemistry of the Eastern Erenhot ophiolitic complex: Implications for the
999 tectonic evolution of the Inner Mongolia-Daxinganling Orogenic Belt. *Journal of*
1000 *Asian Earth Sciences* 97, 279–293.
- 1001 Zhang Z.C., Mao J.W., Chai F.M., Yan S.H., Chen B.L., and Pirajno F. (2009)
1002 Geochemistry of the Permian Kalatongke mafic intrusions, northern Xinjiang,
1003 northwest China: implications for the genesis of magmatic Ni-Cu sulfide deposits.
1004 *Economic Geology* 104, 185–203.
- 1005 Zhao Y., Xue C., Liu S., Symons D.T.A., Zhao X., Yang Y., and Ke J. (2017) Copper
1006 isotope fractionation during sulfide-magma differentiation in the Tulaergen
1007 magmatic - Cu deposit, NW China. *Lithos* 286–287, 206–215.

- 1008 Zhao Y., Xue C.J., Zhao X.B., Yang Y.Q., Ke J.J., Zu B., and Zhang G.Z. (2016) Origin
1009 of anomalously Ni-rich parental magmas and genesis of the Huangshannan Ni-Cu
1010 sulfide deposit, Central Asian Orogenic Belt, Northwestern China. *Ore Geology*
1011 *Reviews* 77, 57–71.
- 1012 Zhou J.B., and Wilde S.A. (2013) The crustal accretion history and tectonic evolution of
1013 the NE China segment of the Central Asian Orogenic Belt. *Gondwana Research* 23,
1014 1365–1377.
- 1015 Zhou M., Leshner C.M., Yang Z., Li J., and Sun M. (2004) Geochemistry and petrogenesis
1016 of 270 Ma Ni-Cu-(PGE) sulfide-bearing mafic intrusions in the Huangshan district,
1017 Eastern Xinjiang, Northwest China: implications for the tectonic evolution of the
1018 Central Asian orogenic belt. *Chemical Geology* 209, 233-257.
- 1019
- 1020

1021 **Figure captions**

1022 Fig. 1. (a) The tectonic context of the central Asian orogenic belt (CAOB) relative to
1023 other Cratons (modified after Jahn et al., 2000). (b) A simplified geological map of the
1024 CAOB (modified after Xiao et al., 2009) showing the mafic-ultramafic intrusions in the
1025 CAOB that formed in arc and post-subduction, extensional settings. (c) A geological map
1026 of the western segment of the CAOB. (d) A geological map of the eastern segment of the
1027 CAOB.

1028

1029 Fig. 2. Chondrite-normalized rare earth element patterns and primitive mantle-normalized
1030 trace element patterns for representative mafic-ultramafic intrusions in the CAOB that
1031 were emplaced in arc settings. Data sources: Jinbulake (Yang and Zhou, 2009), Heishan
1032 (Xie et al., 2012), Erbutu (Peng et al., 2013). Chondrite and primitive mantle values are
1033 from Sun and McDonough (1989).

1034

1035 Fig. 3. Chondrite-normalized rare earth element patterns and primitive mantle-normalized
1036 trace element patterns for representative mafic-ultramafic intrusions in the CAOB that
1037 were emplaced in post-subduction, extensional settings. Data sources: Huangshanxi (Mao
1038 et al., 2014), Hongqiling No.2 (Wei, 2013), and Luodong (Su et al., 2011). Chondrite and
1039 primitive mantle values are from Sun and McDonough (1989).

1040

1041 Fig. 4. Plot of Mg# versus Cr# (a) and Mg# versus XFe^{3+} (b) for the spinel of the mafic-
1042 ultramafic intrusions in the CAOB, and the Dali picrite from the Emeishan large igneous
1043 province. Data sources: Jinbulake, Erbutu, Huangshannan and Tulaergen intrusions (this
1044 study), Heishan intrusion (Wang, 2011), Baixintan intrusion (this study; Feng et al.,
1045 2017), Luodong intrusion (Su et al., 2011), Hongqiling No.1 and No.2 intrusions (Cao et
1046 al., 2019; Wei et al., 2019), Dali picrite (Kamenetsky et al., 2012; Liu et al., 2017).

1047

1048 Fig. 5. Histogram of $\delta^{34}S$ values of sulfides from the Jinbulake, Erbutu, Baixintan and
1049 Tulaergen intrusions in the CAOB. The $\delta^{34}S$ values of MORB-type mantle are from
1050 Labidi et al. (2014).

1051

1052 Fig. 6. Variation of V/Sc of the primary magma against the degrees of partial melting (F)
1053 at given fO_2 (Lee et al., 2005). It is assumed that the mafic-ultramafic intrusions in the
1054 CAOB were derived from magmas produced by ~15 to ~20% of partial melting
1055 (indicated by the grey shaded area) of the mantle wedge in the spinel stability field.

1056

1057 Fig. 7. Plot of XCr^{3+} of spinel versus $\ln Kd_{Mg/Fe}^{Ol-Spl}$ for the mafic-ultramafic intrusions in
1058 the CAOB, and the Dali picrite in the Emeishan large igneous province. Data sources are
1059 the same as those in Fig. 4.

1060

1061 Fig. 8. (a) Comparison of the estimated magma fO_2 of the mafic-ultramafic intrusions in
1062 the CAOB and the Dali picrite in the Emeishan large igneous province with the fO_2 of
1063 MORBs (FMQ-1 to FMQ+0.5) and arc basalts (FMQ+0.5 to FMQ+6). Data sources:
1064 MORBs (Cottrell and Kelley, 2011; Zhang et al., 2018), arc basalts (Woodland et al.,
1065 2006). (b) Plot of the magma fO_2 versus the Fo contents of olivine for the mafic-
1066 ultramafic intrusions in the CAOB and the Dali picrite in the Emeishan large igneous
1067 province. The error bar in (b) represents the uncertainty (FMQ \pm 0.4) of calculated magma
1068 fO_2 based on the olivine-spinel oxygen barometer (*c.f.*, Ballhaus et al., 1991). The dashed
1069 line outlines the data for the intrusions with tholeiitic, parental magmas.

1070

1071 Fig. 9. (a) Comparison of the magma fO_2 calculated based on olivine-spinel oxygen
1072 barometer and the partitioning of V in olivine showing the good agreement of the results
1073 obtained by two different methods. The error bars represent the uncertainty of magma fO_2
1074 calculated based on the two methods. (b) Plot of the magma fO_2 calculated based on the
1075 olivine-spinel oxygen barometer versus the V/Sc of olivine. There is an overall negative
1076 relationship between the magma fO_2 and the V/Sc of olivine. The error bar represents 1 σ
1077 standard deviation of the measured V/Sc of olivine.

1078

1079 Fig. 10. Plot of Al_z (percentage of tetrahedral sites occupied by Al) versus wt.% TiO₂ of
1080 clinopyroxene from the mafic-ultramafic intrusions in the CAOB and the Emeishan large

1081 igneous province. The trends of the arc and rift cumulate are modified after Loucks
1082 (1990).

1083

1084

1085 Fig. 11. Comparison of $\delta^{34}\text{S}$ values of sulfides and magma $f\text{O}_2$ among the mafic-
1086 ultramafic intrusions in the CAOB, the Jinchuan Ni-Cu sulfide deposits in the southern
1087 margin of the North China Craton, and the Ni-Cu sulfide deposits in the Emeishan large
1088 igneous province. The mafic-ultramafic intrusions in the CAOB overall have
1089 $f\text{O}_2 > \text{FMQ}+1$ and $\delta^{34}\text{S}$ similar to the MORB mantle value (-1.6 to +0.6‰; Labidi et al.,
1090 2013, 2014), whereas the Ni-Cu sulfide deposits in the intraplate settings have relatively
1091 low $f\text{O}_2$ and high $\delta^{34}\text{S}$ of sulfides. Data sources: Jinbulake, Erbutu, Baixintan and
1092 Tulaergen intrusions (this study), Heishan intrusion (Xie et al., 2014), Hongqiling No.7
1093 intrusion (Wei et al., 2019), Luodong intrusion (Su et al., 2015), Poyi intrusion (Xia et al.,
1094 2013), Huangshannan intrusion (Zhao et al., 2016), Huangshandong and Huangshanxi
1095 intrusions (Wang et al., 1987), Jinchuan intrusion (Ripley et al., 2005; Duan et al., 2016),
1096 the intrusions in the Emeishan large igneous province (Wang et al., 2018).

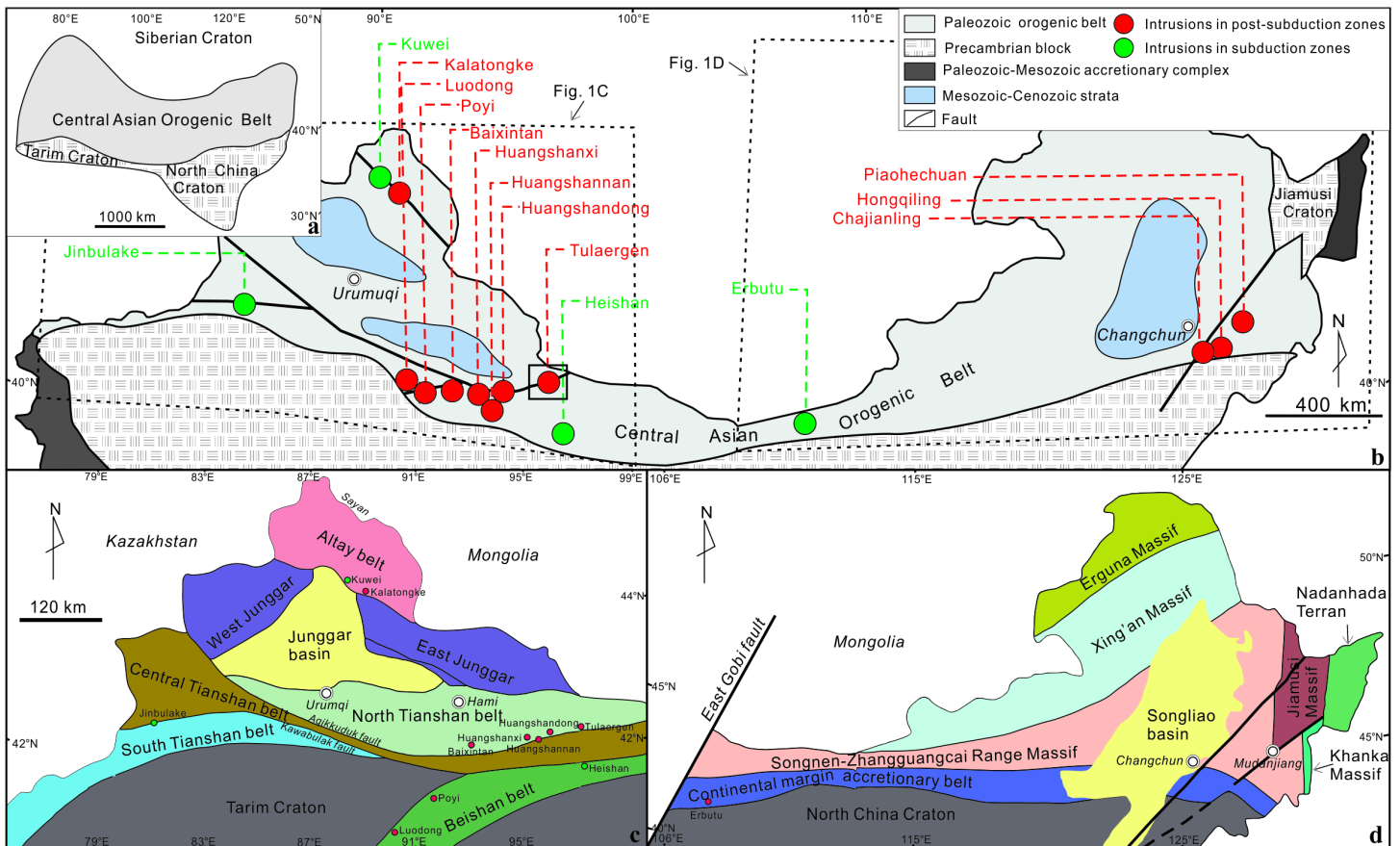
1097

1098 Fig. 12. Comparison of magma $f\text{O}_2$ values calculated based on the olivine-spinel oxygen
1099 barometer with those calculated based on the Fe-Ni exchange between olivine and sulfide
1100 melt for the Baixintan (BXT), Huangshannan (HSN), Huangshandong (HSD),
1101 Huangshanxi (HSX), Tulaergen (TLEG), and Hongqiling No.1 (HQL) intrusions in the
1102 CAOB. The values based on the Fe-Ni exchange between olivine and sulfide liquids are
1103 much lower than those based on the olivine-spinel oxygen barometer.

Table 1 S isotopic compositions of the sulfides in the rocks from the Jinbulake, Erbutu, Baixintan and Tulaergen intrusions in the central Asian orogenic belt

Analysis No.	Sample No.	Sulfides	$\delta^{34}\text{S}\%$ (V-CDT)	Analysis No.	Sample No.	Sulfides	$\delta^{34}\text{S}\%$ (V-CDT)
Jinbulake intrusion				15	18EBT-11	pentlandite	6.2
1	QB-13	pyrrhotite	0.6	16	18EBT-11	pyrrhotite	6.2
2	QB-13	pyrrhotite	0.3	17	18EBT-11	pyrrhotite	6.4
3	QB-13	pyrrhotite	0.0	18	18EBT-5	pentlandite	5.5
4	QB-13	pyrrhotite	0.5	19	18EBT-5	pentlandite	5.5
5	QB-13	pyrrhotite	0.9	20	18EBT-5	pyrrhotite	5.8
6	QB2-102	pyrrhotite	0.9	21	18EBT-5	pyrrhotite	5.3
7	QB2-102	pyrrhotite	0.8	22	18EBT-5	pyrrhotite	5.6
8	QB2-102	pyrrhotite	0.8	23	18EBT-5	chalcopyrite	6.0
9	QB2-102	pyrrhotite	1.3	24	18EBT-5	pentlandite	6.0
10	QB2-78	pyrrhotite	0.1	25	18EBT-5	pentlandite	5.6
11	QB2-78	pyrrhotite	0.2	Baixintan intrusion			
12	QB2-78	pyrrhotite	0.7	1	19BXT-4	chalcopyrite	0.4
13	QB2-78	pyrrhotite	0.5	2	19BXT-4	chalcopyrite	0.3
14	QB-43	pyrrhotite	0.3	3	19BXT-4	pyrrhotite	-0.1
15	QB-43	pentlandite	0.3	4	19BXT-4	pyrrhotite	0.5
16	QB-43	pentlandite	0.3	5	19BXT-4	chalcopyrite	1.1
17	QB-43	pyrrhotite	0.6	6	19BXT-6	pyrite	0.7
18	QB-43	pyrrhotite	0.7	7	19BXT-6	pyrite	0.5
19	QB-43	pentlandite	0.6	8	19BXT-6	pyrite	0.6
20	QB-43	pyrrhotite	0.7	9	19BXT-14	chalcopyrite	0.6
21	QB-65	chalcopyrite	0.9	10	19BXT-14	chalcopyrite	0.1
22	QB-65	chalcopyrite	0.9	11	19BXT-14	pyrrhotite	-0.7
23	QB-65	pyrrhotite	0.6	12	19BXT-14	pyrrhotite	0.1
24	QB-65	pyrrhotite	0.4	13	19BXT-ZK-15	chalcopyrite	1.2
25	QB-65	chalcopyrite	1.3	14	19BXT-ZK-15	pyrrhotite	0.0
26	QB-65	pentlandite	0.7	15	19BXT-ZK-15	chalcopyrite	-0.4
27	QB-65	pyrrhotite	0.9	16	19BXT-ZK-15	chalcopyrite	0.2
28	QB-65	pyrrhotite	0.6	17	19BXT-ZK-15	chalcopyrite	-0.1
Erbutu intrusion				18	19BXT-ZK-15	pentlandite	-0.3
1	18EBT-10	pyrrhotite	7.5	19	19BXT-ZK-15	pentlandite	-0.4
2	18EBT-10	pyrrhotite	7.4	Tulaergen intrusion			
3	18EBT-10	chalcopyrite	7.3	1	TLEG-16	pyrrhotite	0.5
4	18EBT-10	chalcopyrite	5.9	2	TLEG-16	pyrrhotite	0.9
5	18EBT-11	chalcopyrite	6.7	3	TLEG-16	pyrrhotite	0.3
6	18EBT-11	pentlandite	6.2	4	TLEG-16	pentlandite	0.4
7	18EBT-11	pentlandite	6.0	5	TLEG-16	pyrrhotite	0.3
8	18EBT-11	chalcopyrite	6.7	6	TLEG-19	pyrrhotite	0.2
9	18EBT-11	chalcopyrite	6.9	7	TLEG-19	pyrrhotite	-0.2
10	18EBT-11	pentlandite	6.2	8	TLEG-19	pyrrhotite	0.3
11	18EBT-11	pentlandite	6.7	9	TLEG-19	pyrrhotite	0.4
12	18EBT-11	chalcopyrite	6.9	10	TLEG-26	chalcopyrite	0.5
13	18EBT-11	pentlandite	6.4	11	TLEG-26	pyrrhotite	0.2
14	18EBT-11	pentlandite	5.9				

Fig. 1



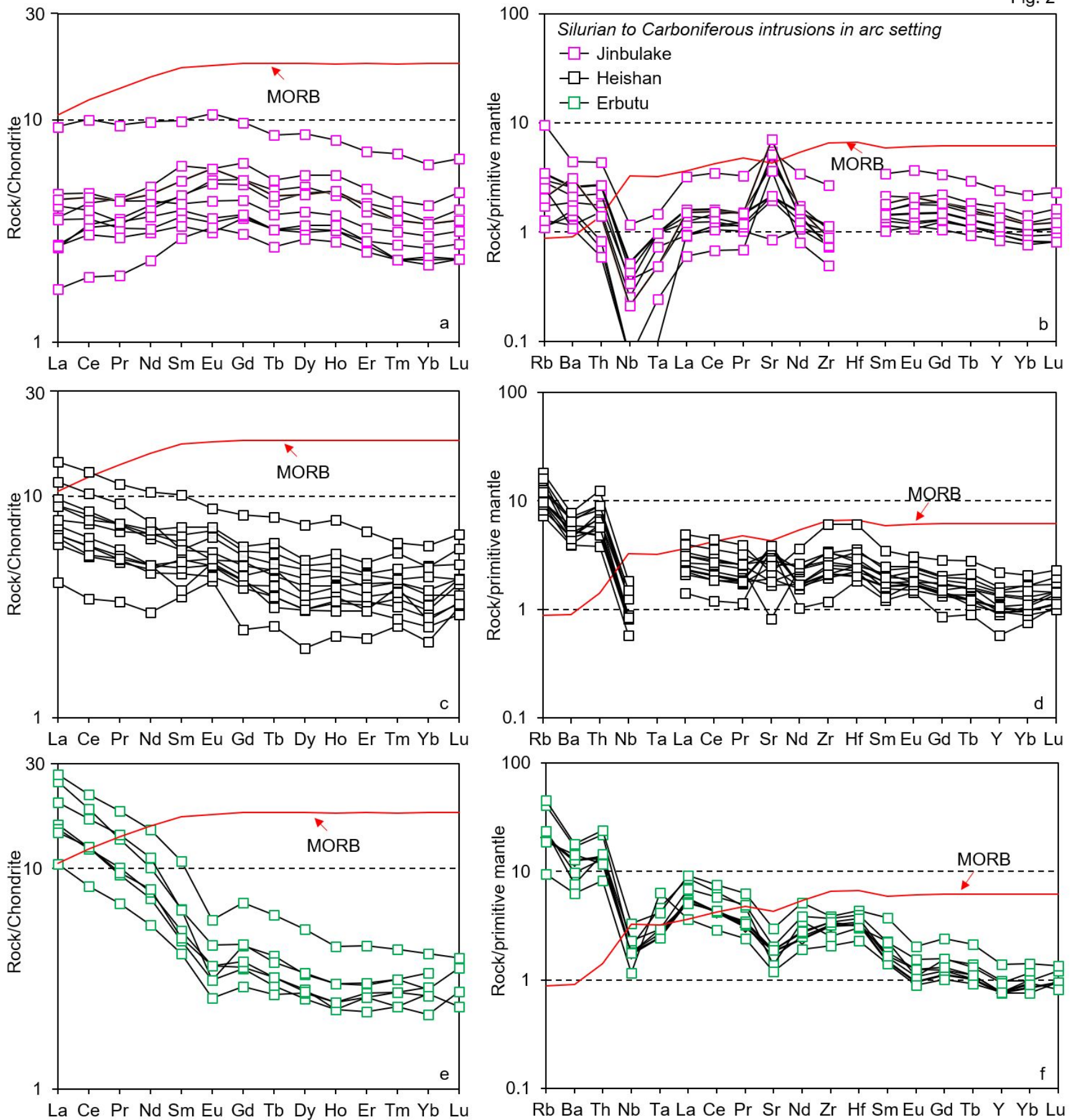
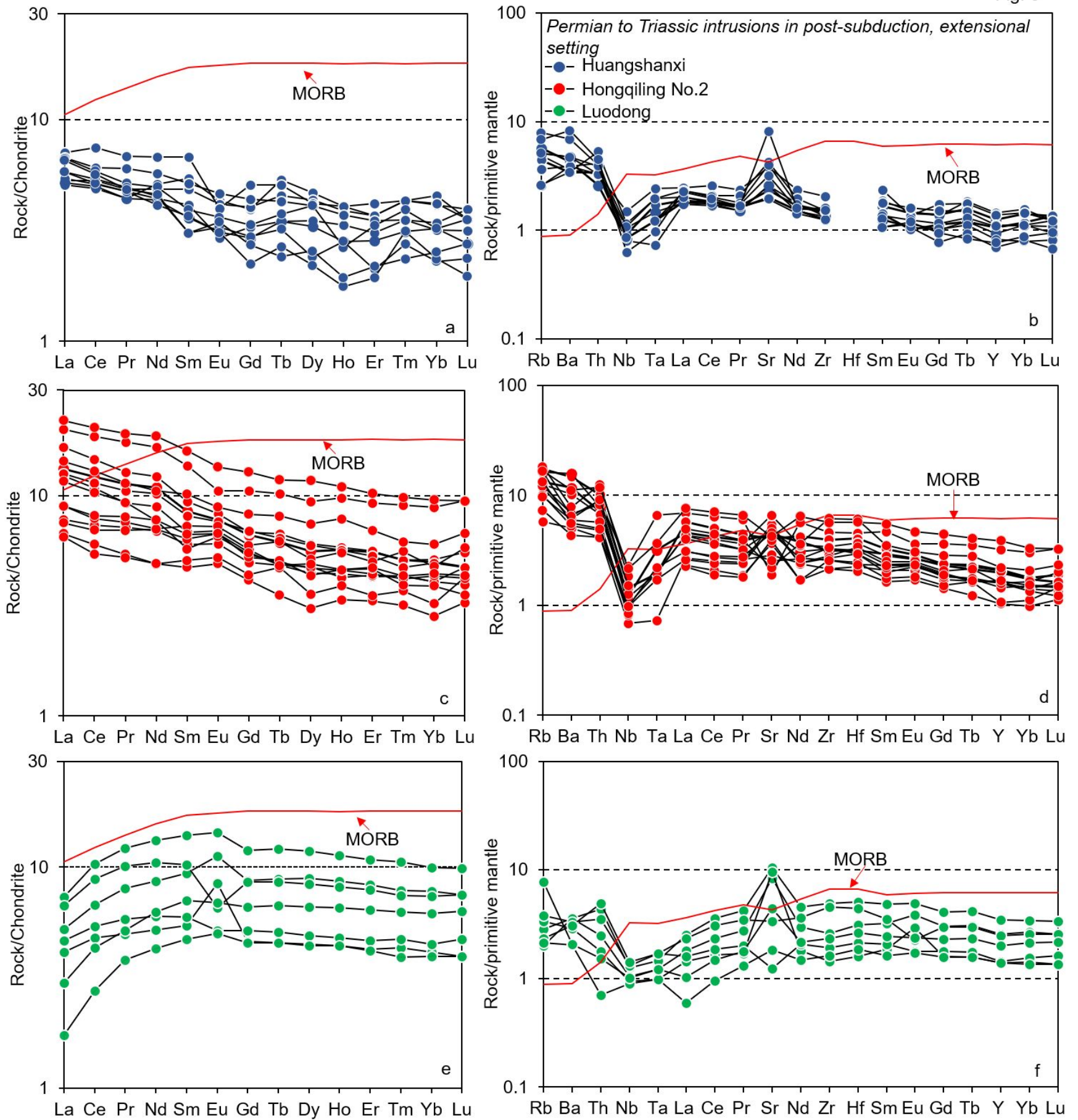


Fig. 3



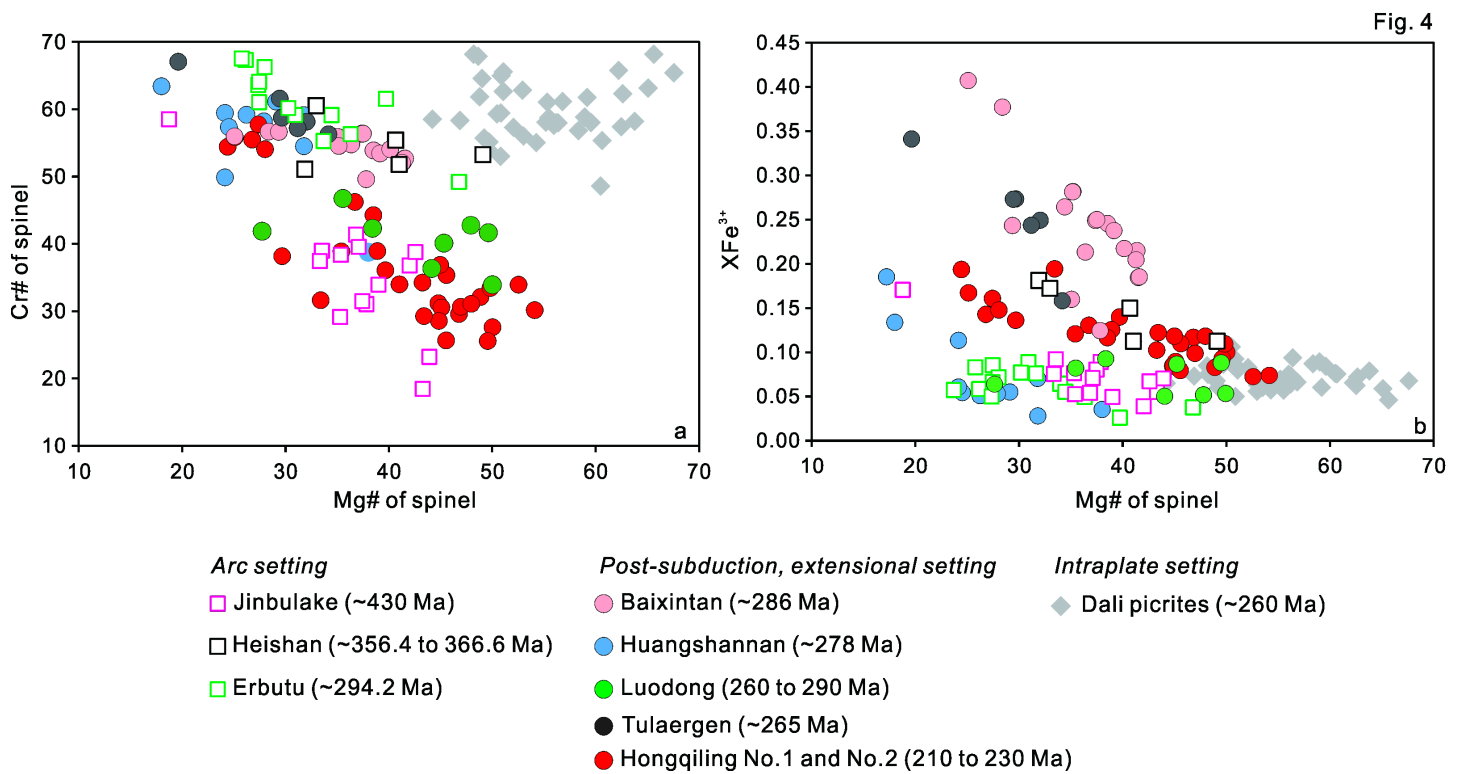


Fig. 5

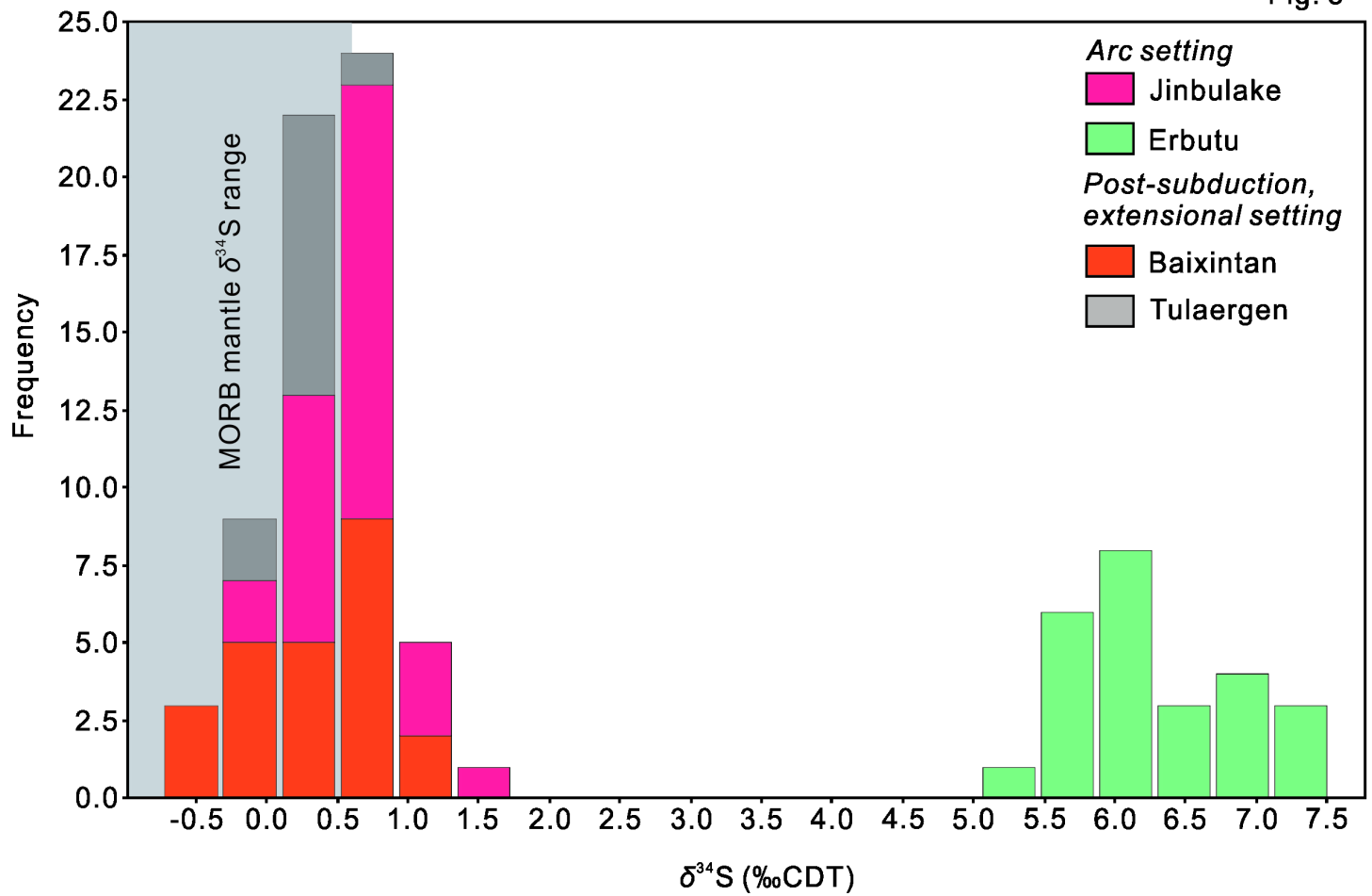


Fig. 6

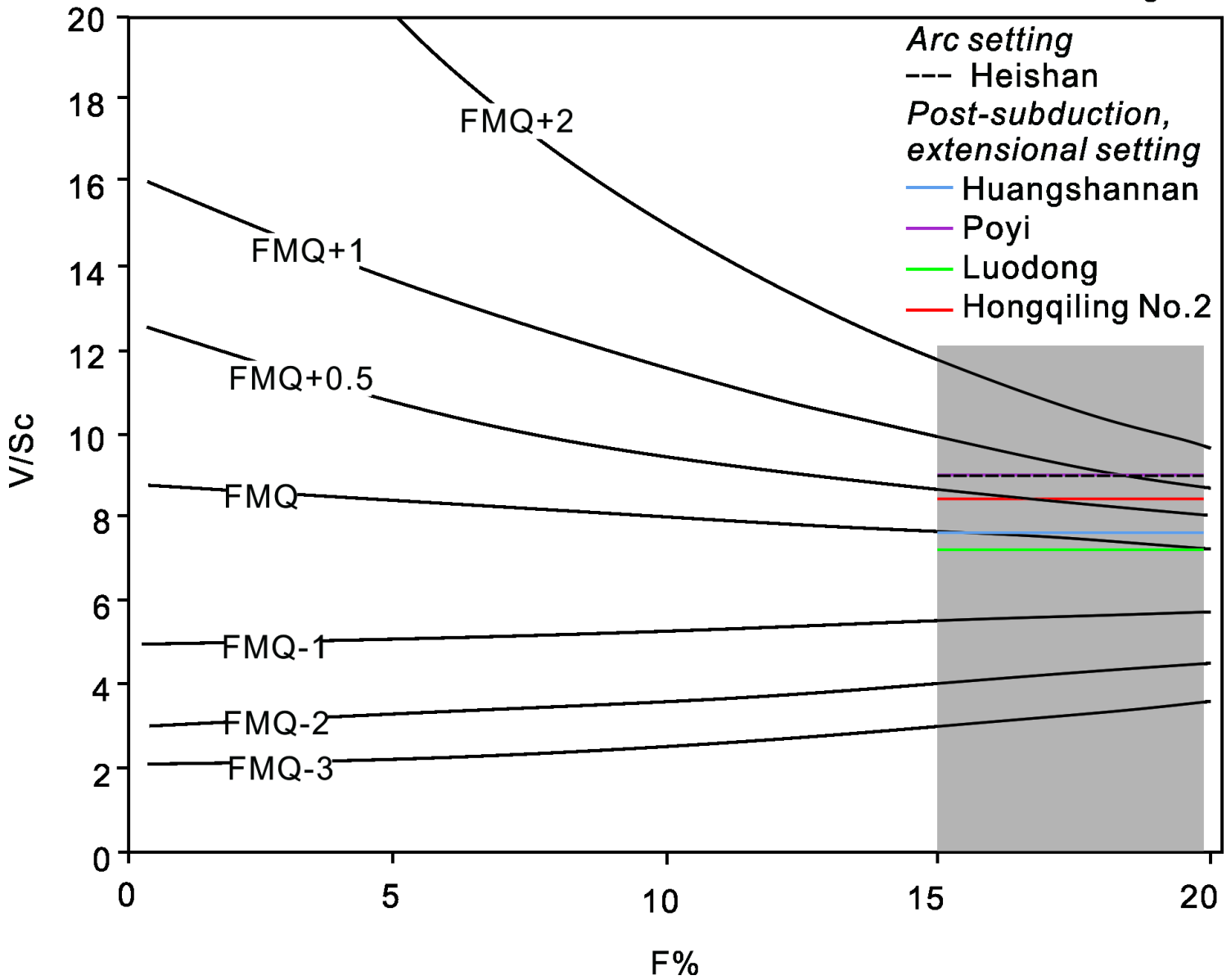


Fig. 7

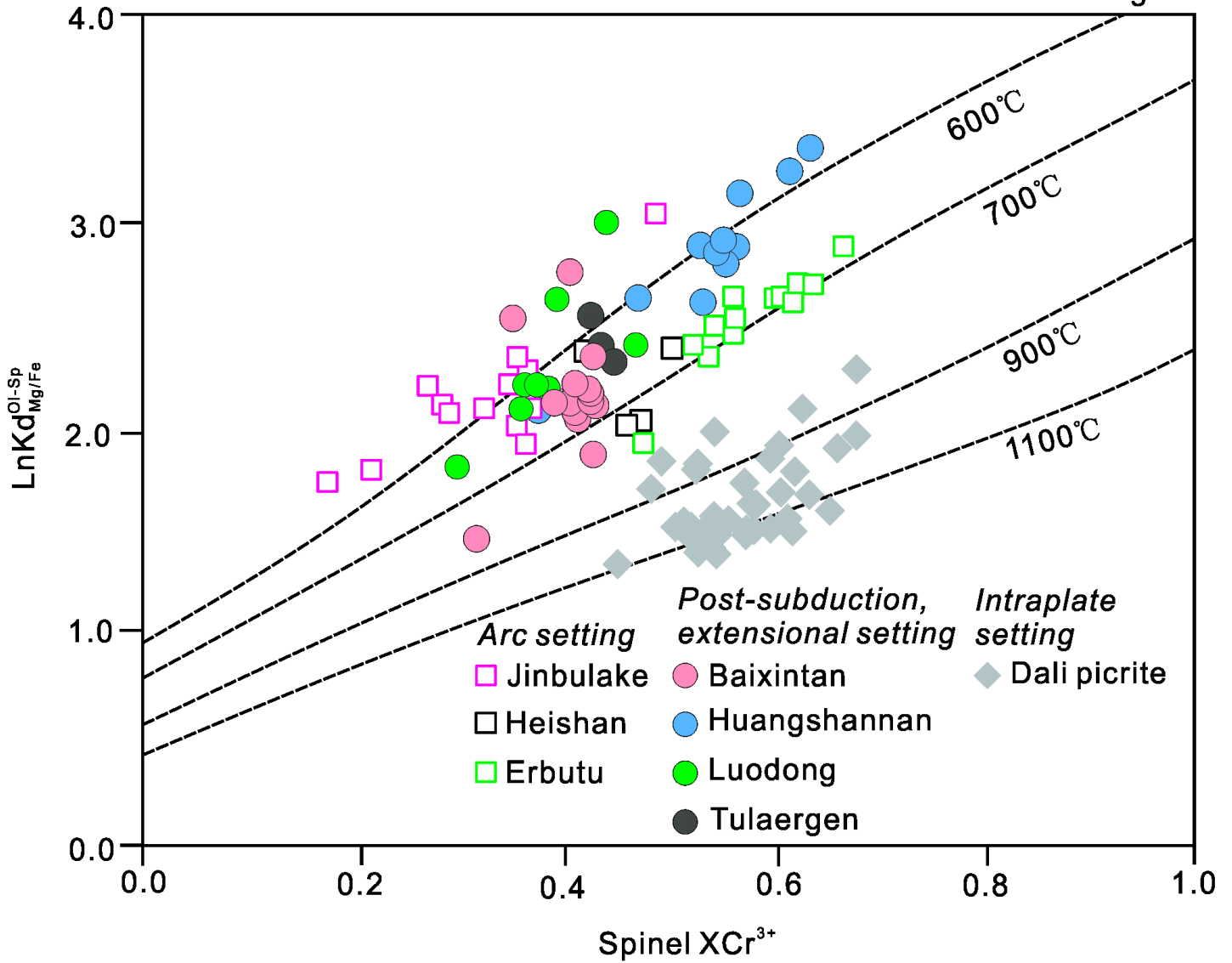
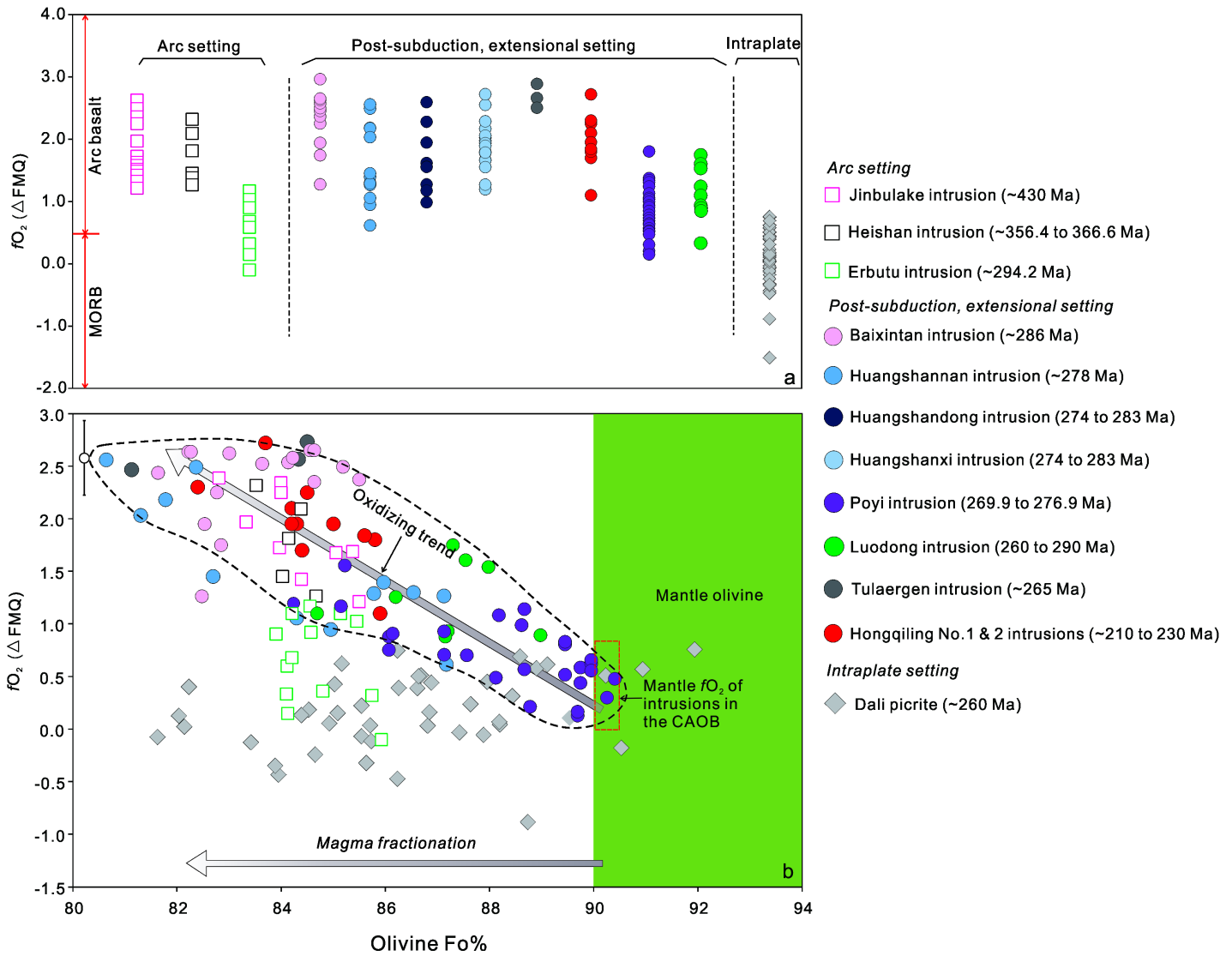


Fig. 8



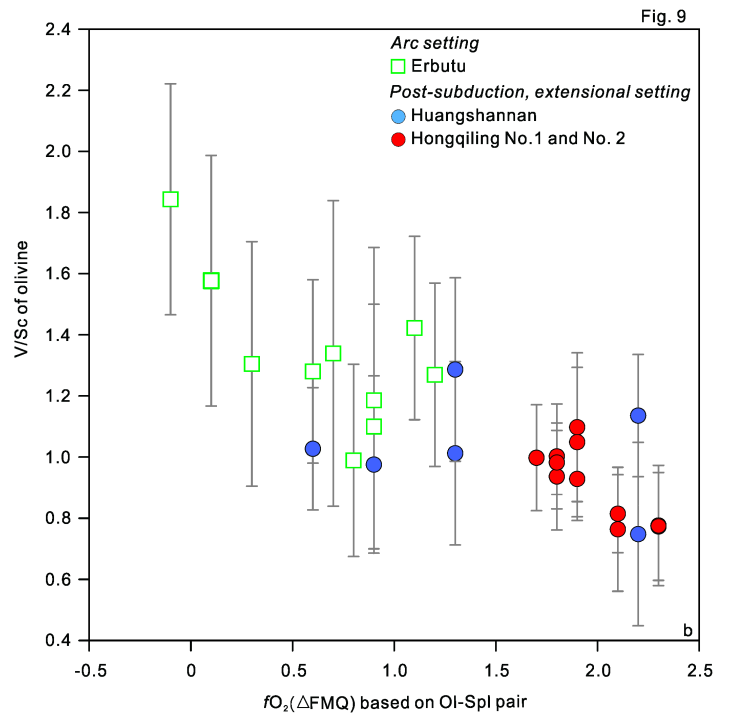
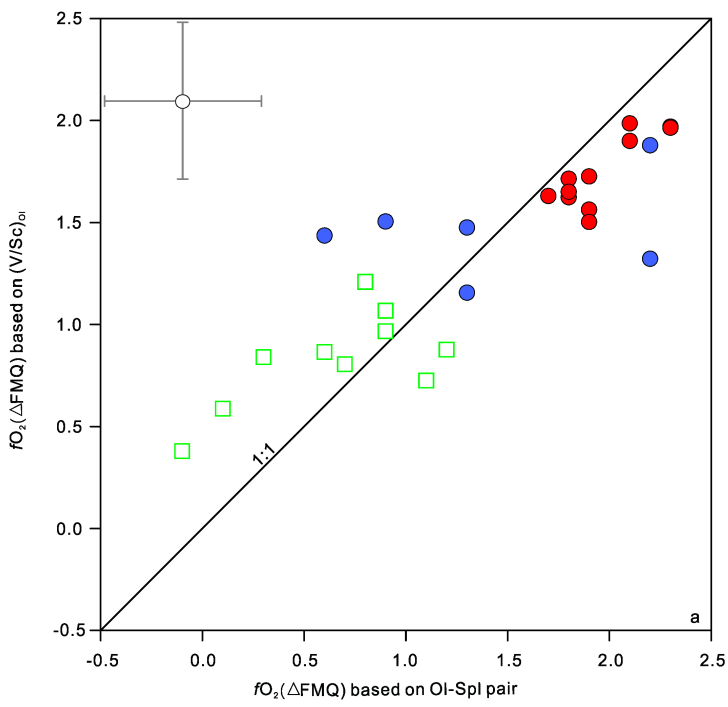


Fig. 10

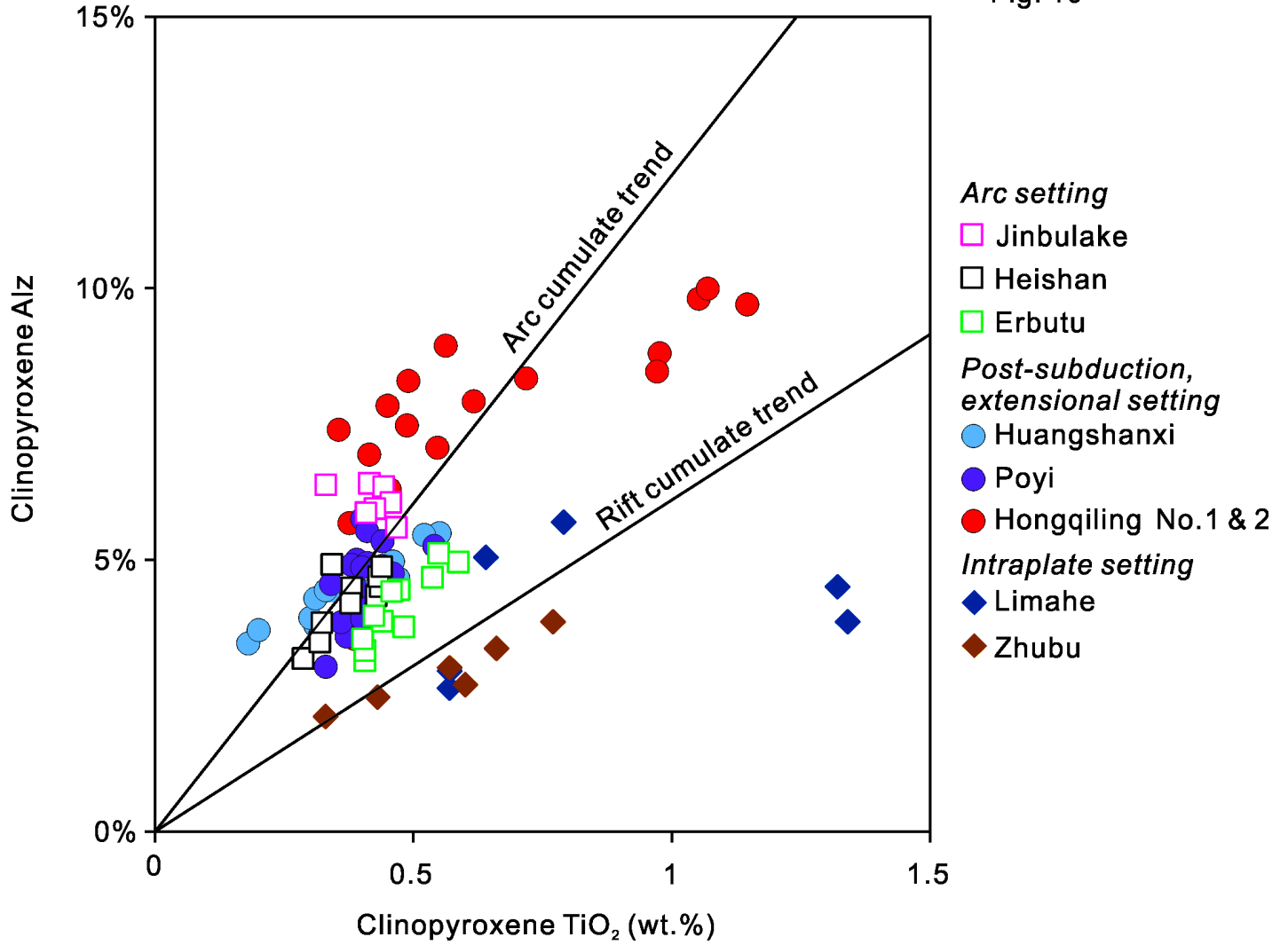


Fig. 11

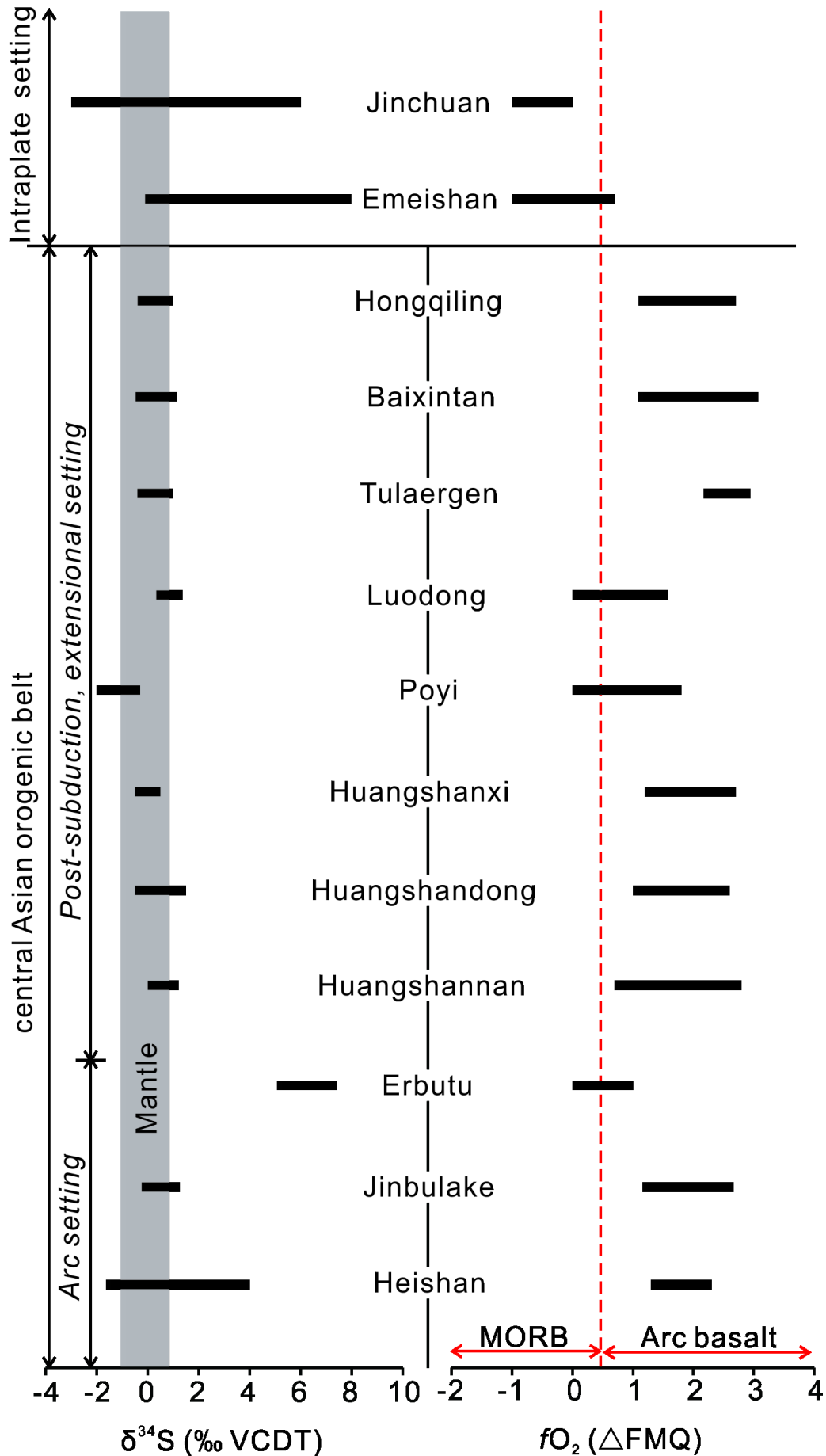


Fig. 12

